

<b>Manuscript Number:</b>	A-25-4993
<b>Article Type:</b>	Full length article
<b>Keywords:</b>	Ion irradiation, TEM, thermal stability, nanoindentation
<b>Corresponding Author:</b>	Skye Supakul Pacific Northwest National Laboratory UNITED STATES OF AMERICA
<b>First Author:</b>	Skye Supakul
<b>Order of Authors:</b>	Skye Supakul Eda Aydogan Mert Efe Matthew Vigil Bochuan Sun Ishtiaque Robin Kayla Yano Wei-Ying Chen Damian Sobieraj Jan Wróbel Duc Nguyen-Manh Enrique Martinez Dan Thoma Stuart Maloy Osman El-Atwani
<b>Abstract:</b>	Vanadium-based alloys such as V-4Cr-4Ti are of interest as candidates for low activation structural materials for advanced nuclear reactors. One of the major challenges of vanadium-based alloys is their thermal stability and improving their mechanical properties at higher temperature ranges (> 600 °C). This work explores refining the grain microstructure of V-4Cr-4Ti by arc melting and subsequently large strain extrusion machining specimens to produce a multimodal microstructure largely composed of nanocrystalline and ultrafine grain sizes. In-situ thermal stability of the multimodal V-4Cr-4Ti to 800 °C shows the formation of vanadium carbides with negligible grain growth. In-situ dual-beam 16 KeV He <sup>+</sup> and 1 MeV Kr <sup>2+</sup> ion irradiation performed at 700 °C to a final dose of ~5 displacements per atom show the formation of small He cavities well distributed throughout the system, with preferential clustering at grain boundaries. This work provides insight into how the increased fraction of grain boundaries affect the simultaneous dual beam ion irradiation response of multimodal V – 4 wt.% Cr – 4 wt.% Ti at elevated temperatures. Analysis of the cavities reveal an areal density of 0.024±0.007 cavities/nm <sup>2</sup> and swelling of 0.236% after the dual-beam ion irradiation. Nanoindentation shows a ~50% increase in hardening after the ion irradiation at 700 °C.
<b>Suggested Reviewers:</b>	Yongqiang Wang yqwang@lanl.gov Matheus Tunes matheus.tunes@unileoben.ac.at Anter El Azab

	aelazab@purdue.edu
	Hyosim Kim hkim@lanl.gov
	Kevin Jacob jkevin@iastate.edu
<b>Opposed Reviewers:</b>	



*Reactor Materials Group, EED*

Pacific Northwest National Laboratory  
PCD 757715, 790 6<sup>th</sup> Street  
Richland, WA 99354

*Date: November 26<sup>th</sup>, 2025*

### **Coordinating Editor of Acta Materialia**

Dear Professor Gregory Rohrer, Coordinating Editor of Acta Materialia,

Enclosed is a Microsoft word file of a manuscript titled, “***Thermal Stability and Ion Irradiation Response of Refined Grained V–4Cr–4Ti***” by Skye Supakul, Eda Aydogan, Mert Efe, Matthew Vigil, Bochuan Sun, Ishtiaque Robin, Kayla Yano, Wei-Ying Chen, Damian Sobieraj, Jan S. Wróbel, Duc Nguyen-Manh, Enrique Martinez, Dan Thoma, Stuart Maloy, and Osman El-Atwani that we would like to have considered for publication in *Acta Materialia*. Alongside the main manuscript, a supplementary word document with additional figures and tables is provided. Supplementary videos of the *in-situ* ion irradiation for the investigated compositions are also provided.

Due to their properties under extreme environments, vanadium-based alloys are of high interest as candidates for structural materials in next generation advanced nuclear reactors. However, part of the challenge associated with vanadium-based alloys in their implementation is their relatively low operating temperature, rated ~600 °C or below. While vanadium-based alloys have demonstrated better high temperature mechanical performance in comparison to steels, at elevated temperatures they have the tendency to form carbides and oxides which can lead to high temperature embrittlement. Thus, significant effort has gone into improving the high temperature stability and properties of vanadium-based alloys. Here in this work, large strain extrusion machining (LSEM) was used to refine the grains of coarse grain, as-cast V-4Cr-4Ti (V44), producing a multimodal grain microstructure with a large area fraction of nanocrystalline ( $d < 100$  nm) and ultrafine grains ( $100 < d < 500$  nm). This refined grade of V44 was investigated through *in-situ* high temperature heating and annealing at 800 °C, *in-situ* dual-beam ion irradiation at 700 °C, and nanoindentation before and after high temperature ion irradiation. Some of the findings are summarized below:

- Complex strain fields due to the increased number of dislocations and grain boundaries from the multi-modal grained sample produced by LSEM is suspected to lead to lower kinetics for the formation of precipitate phases and grain growth as observed by the slower activity observed in the LSEM V44 when exposed to high temperatures in the *in-situ* heating and *in-situ* dual-beam ion irradiation experiments as compared to the coarse grain specimen

- The observation of carbides at high temperatures as well as before and after dual-beam ion irradiation of the LSEM V44 at elevated temperature shows little changes to their morphology, suggesting their formation is thermally driven rather than irradiation induced.
- The presence of smaller sized carbides in the LSEM V44 after high temperatures may be attributed to the large number and widespread distribution of dislocations, serving to distribute impurities throughout the system and inhibiting their coalescence into larger carbides.
- The LSEM V44 and coarse grain V44 possess similar ion irradiation properties in terms of cavity density and size suggesting grain boundaries are not playing a major role in the ion irradiation tolerance of V44
- LSEM ( $3.25 \pm 0.30$  GPa) exhibited a  $\sim 50\%$  increase in hardness ( $5.00 \pm 0.54$  GPa) after the dual-beam ion irradiation at  $700\text{ }^\circ\text{C}$  to 5 dpa likely due to the presence of hard precipitate phases as well as ion irradiation induced cavities serving as hard obstacles to impede dislocation movement during nanoindentation.

The multi-modal, grain refined V44 processed by LSEM studied here discusses key insights into the thermal stability, ion irradiation behavior, and mechanical properties, correlated to its microstructure by utilizing in-situ TEM characterization techniques.

The authors declare that none of the material has been previously published or is under consideration for publication elsewhere, and the authors have no competing conflicts of interest.

On behalf of my co-authors, I thank you for your consideration of this manuscript.

Sincerely,  
Dr. Skye Supakul



Pacific Northwest National Laboratory

[Click here to view linked References](#)

1  
2  
3  
4  
5  
6  
7  
8  
9  
10  
11  
12  
13  
14  
15  
16  
17  
18  
19  
20  
21  
22  
23  
24  
25  
26  
27  
28  
29  
30  
31  
32  
33  
34  
35  
36  
37  
38  
39  
40  
41  
42  
43  
44  
45  
46  
47  
48  
49  
50  
51  
52  
53  
54  
55  
56  
57  
58  
59  
60  
61  
62  
63  
64  
65

# 1 Thermal Stability and Ion Irradiation Response of Refined Grained V – 4Cr – 2 4Ti

## 3 4 **Authors:**

5 Skye Supakul<sup>a\*</sup>, Eda Aydogan<sup>a</sup>, Mert Efe<sup>a</sup>, Matthew Vigil<sup>b</sup>, Bochuan Sun<sup>c</sup>, Ishtiaque Robin<sup>a</sup>, Kayla  
6 Yano<sup>a</sup>, Wei-Ying Chen<sup>d</sup>, Damian Sobieraj<sup>e</sup>, Jan S. Wróbel<sup>e</sup>, Duc Nguyen-Manh<sup>f,g</sup>, Enrique  
7 Martinez<sup>c,h</sup>, Dan Thoma<sup>b</sup>, Stuart Maloy<sup>a</sup>, Osman El-Atwani<sup>a</sup>

## 8 **Affiliations:**

9 <sup>a</sup> Pacific Northwest National Laboratory, Richland, WA, USA

10 <sup>b</sup> University of Wisconsin-Madison, Department of Materials Science and Engineering, Madison,  
11 WI, USA

12 <sup>c</sup> Department of Materials Science and Engineering, Clemson University, Clemson, SC, USA

13 <sup>d</sup> Argonne National Laboratory, Lemont, IL, USA

14 <sup>e</sup> Faculty of Materials Science and Engineering, Warsaw University of Technology, Poland

15 <sup>f</sup> Materials Division, United Kingdom Atomic Energy Authority, Culham Campus, Abingdon,  
16 United Kingdom

17 <sup>g</sup> Department of Materials, University of Oxford, Parks Road, United Kingdom

18 <sup>h</sup> School of Mechanical and Automotive Engineering, Clemson University, Clemson, SC, USA

19 \*Corresponding author: Skye Supakul ([skye.supakul@pnnl.gov](mailto:skye.supakul@pnnl.gov)), Osman El-Atwani  
20 ([osman.elatwani@pnnl.gov](mailto:osman.elatwani@pnnl.gov))

## 21 **Abstract**

22 Vanadium-based alloys such as V-4Cr-4Ti are of interest as candidates for low activation structural  
23 materials for advanced nuclear reactors. One of the major challenges of vanadium-based alloys is  
24 their thermal stability and improving their mechanical properties at higher temperature ranges (>  
25 600 °C). This work explores refining the grain microstructure of V-4Cr-4Ti by arc melting and  
26 subsequently large strain extrusion machining specimens to produce a multimodal microstructure  
27 largely composed of nanocrystalline and ultrafine grain sizes. *In-situ* thermal stability of the  
28 multimodal V-4Cr-4Ti to 800 °C shows the formation of vanadium carbides with negligible grain  
29 growth. *In-situ* dual-beam 16 KeV He<sup>+</sup> and 1 MeV Kr<sup>2+</sup> ion irradiation performed at 700 °C to a  
30 final dose of ~5 displacements per atom show the formation of small He cavities well distributed  
31 throughout the system, with preferential clustering at grain boundaries. This work provides insight  
32 into how the increased fraction of grain boundaries affect the simultaneous dual beam ion  
33 irradiation response of multimodal V – 4 wt.% Cr – 4 wt.% Ti at elevated temperatures. Analysis  
34 of the cavities reveal an areal density of 0.024±0.007 cavities/nm<sup>2</sup> and swelling of 0.236% after  
35 the dual-beam ion irradiation. Nanoindentation shows a ~50% increase in hardening after the ion  
36 irradiation at 700 °C.

37 **Keywords:** Ion irradiation, TEM, thermal stability, nanoindentation

## 1. Introduction

Since the 1960s, there has been significant interest in vanadium-based alloys as low-activation materials for nuclear reactor operations. Initially considered as candidates for liquid metal-cooled fast reactors, vanadium-based alloys have recently gained renewed attention as alternatives to reduced activation ferritic/martensitic (RAFM) steels for first wall and blanket materials in fusion energy systems due to their limited operating regimes [1-6]. Vanadium-based alloys, such as V-4Cr-4Ti (V44), exhibit desirable thermo-mechanical properties, including a higher melting temperature and promising thermal conductivity compared to other candidate materials like 316 stainless steel (SS) and HT-9 [7]. With the low neutron absorption cross-section of V44, it has also been proposed in self-cooled vanadium (V)/lithium (Li) blanket design concepts, which can achieve the necessary tritium breeding ratio required for sustained reactor operation without requiring the addition of beryllium (Be) [6]. In terms of radioactivity and afterheat decay, high-purity V44 is generally categorized as Class A waste, decaying to acceptable levels during site occupancy. In contrast, V44 of commercial quality or lower purity could be classified as Class B or Class C nuclear waste, which stabilizes and decays to safe levels within 100 years or 500 years, respectively.

In addition to promising neutronic properties, V44 also possesses a low thermal expansion coefficient across various temperatures. However, V44 alloys have exhibited susceptibility to embrittlement with high levels of hydrogen and oxygen, as well as a reduction in elongation and irradiation work hardening which have largely been attributed to the formation of high densities of irradiation defects and precipitates [8, 9]. Also, the mechanical properties of vanadium-based alloys can vary significantly due to the presence of impurities such as carbon (C), oxygen (O), and nitrogen (N) [10]. Fine precipitates of vanadium carbide [11] and Ti (C, O, N) [9, 12, 13] have been reported in the literature, forming after heat treatment and irradiation at elevated temperatures. Consequently, extensive research has focused on investigating the effects of impurities and controlling their levels [9, 14-16]. Furthermore, studies have explored the influence of various elements and particles, such as Fe, Si, ZrC, TiC, Ti<sub>3</sub>SiC<sub>2</sub>, and Y-based oxides, on strength, ductility, and creep resistance [15, 17, 18]. Others have also investigated the thermo-mechanical processing of V44 through aging, deformation, and annealing [9, 11, 12, 19], observing banded microstructures with fine grains, alongside the formation of precipitates as a result of aging. The formation of these bands leads to inhomogeneities in the mechanical performance of the system. When subjected to ion irradiation at elevated temperatures, the microstructure can become unstable due to the breakdown of Ti (C, O, N) and the formation of V (C, O, N), attributed to the redistribution of carbon throughout the system.

To implement vanadium-based alloys as structural materials, further work is required to modify the microstructure and control the impurity content in the system. In addition, there is significant interest in the community to improve the operating temperature window of vanadium alloys, aiming to improve their high temperature strength and creep properties [6]. Apart from different alloying additions and oxide or precipitate strengthening, microstructural modifications serve as another technique to improve the performance of a material. Various groups have employed a series of multi-step thermomechanical treatments (TMT) to modify V44 [11, 20-22]. Moreover, there has been only a limited number of studies discussing the ion irradiation behavior of ultrafine-grained or nanocrystalline V44 [11]. Work on modifying tungsten to produce nanocrystalline grains using large strain extrusion machining (LSEM) has demonstrated reductions in the areal density of helium cavities, defect clusters, and dislocations, as compared to ultrafine-grained

1  
2  
3  
4 83 tungsten [23, 24]. Additionally, increased strength, while retaining much of the ductility, has been  
5 84 observed with grain and precipitate refinement in TMT modified V44 [21]. Thus, the present study  
6 85 utilized LSEM to refine the grain microstructure of V44, producing LSEM V44 with a multimodal  
7 86 grain size distribution, ranging from nanocrystalline to coarse grain sizes. *In-situ* high-temperature  
8 87 transmission electron microscopy (TEM) investigations were performed to gain insight into the  
9 88 thermal stability of nanocrystalline V44 at temperatures up to 800 °C. Furthermore, simultaneous  
10 89 dual-beam ion irradiation using 16 keV He<sup>+</sup> and 1 MeV Kr<sup>2+</sup> at an elevated temperature of 700 °C  
11 90 was conducted to evaluate the irradiation tolerance of multimodal grain-sized V44.  
12 91 Nanoindentation was performed before and after irradiation to investigate the ion irradiation  
13 92 hardening behavior, revealing a ~50% increase in hardening after ion irradiation.

## 17 93 **2. Materials and Methods**

### 18 94 *2.1 Arc Melting and LSEM of V – 4 wt.% Cr – 4 wt.% Ti*

19 94 Ingots were prepared by arc-melting using an Arcast Arc 200. Shot of pure elements of V (99.9%),  
20 95 Ti (99.9%), and Cr (99.95%) were melted together on a water-cooled copper crucible in an ultra-  
21 96 high purity Ar (99.999%) environment. The chamber was evacuated to ~2.7x10<sup>-4</sup> kPa and back-  
22 97 filled to ~35 kPa with ultra-high purity Ar three times to minimize O and N contamination. In  
23 98 addition, a Ti getter ingot was melted prior and adjacent to the ingots. This process was repeated  
24 99 at least four times, flipping the ingot each time to ensure complete mixing. The Ti getter and  
25 100 samples were lustrous with no discoloration and minimal mass lost between melts. The final  
26 101 weight of the ~1” dia. ingot was approximately 40g. Initial microstructure of the coarse grain (CG)  
27 102 arc melted specimen is shown in [Supplemental Figure S1](#), with grain size diameters on the order  
28 103 of several hundred microns.  
29 104

30 105 Nanocrystalline V44 alloy chips and semi-continuous strips were produced by the large strain  
31 106 extrusion machining (LSEM) process, which peeled/machined the chips from the as-cast V44  
32 107 buttons in a lathe. With LSEM, large strains can be imposed in a narrow and confined shear  
33 108 deformation zone between the cutting tools to refine microstructures to the ultrafine and  
34 109 nanocrystalline level. The other thermo-mechanical conditions such as strain rate and temperature  
35 110 can also be modeled and controlled in the deformation zone as accurate as strain. Since machining  
36 111 is a high strain rate process by its nature, adiabatic heating due to the large plastic deformation can  
37 112 cause a local temperature rise in the deformation zone. The temperature rise in the deformation  
38 113 zone was calculated and reported, even though all the machining was done at room temperature  
39 114 without the preheating of the disc [25].

40 115 The effective strain  $\bar{\epsilon}$  imposed on the strips can be calculated by equation 1 which idealizes the  
41 116 deformation zone as a single shear plane:

$$42 117 \bar{\epsilon} = \frac{\gamma}{\sqrt{3}} \quad (1)$$

43 118 where  $\gamma$  is the shear strain. Shear strain is calculated by using equation 2 below:

$$44 119 \gamma = \frac{\lambda}{\cos \alpha} + \frac{1}{\lambda \cos \alpha} - 2 \tan \alpha \quad (2)$$

45 120 where  $\alpha$  is the tool rake angle and  $\lambda$  is the chip or strip thickness ratio. The strip thickness ratio is  
46 121  $t_c/t_0$ , where  $t_c$  and  $t_0$  are the final and the uniformed chip thicknesses respectively. In LSEM, an  
47 122 optional constraining tool can be used to control the final strip thickness. There was no constraining

1  
2  
3  
4 123 tool used in this study, and the final strip thickness naturally formed as a result of the shear strain  
5 124 imposed on the material and its relative ductility.

7 125 Strain rate  $\dot{\epsilon}$  is approximated using a deformation zone thickness ( $\Delta$ ) and deformation speed ( $V$ ) in  
8 126 equation 3 below:

$$\dot{\epsilon} \sim \frac{\bar{\epsilon}V}{\Delta} = \frac{\gamma V}{\sqrt{3}\Delta}. \quad (3)$$

10  
11 127  
12  
13  
14 128 The average deformation zone temperature ( $T$ ) can be estimated using the shear plane model which  
15 129 converts the cutting energy to the adiabatic deformation heating and calculates the fraction of heat  
16 130 flowing into the work material by considering the work material's heat capacity, thermal  
17 131 conductivity, density, and the shear plane component of the cutting force. The physical properties  
18 132 used to calculate the temperature are based on the reported values for pure vanadium, where heat  
19 133 capacity,  $C = 0.49$  J/gK, thermal conductivity,  $\kappa = 35$  W/mK, and density,  $\rho = 6.11$  g/cm<sup>3</sup>. The  
20 134 specific cutting energy ( $u_s$ ) was assumed to be similar to steels with  $u_s = 2.9 \times 10^9$  J/m<sup>3</sup>. **Table 1**  
21 135 summarizes the process parameters used in this study and the strain, strain rate, and temperature  
22 136 that the strip experienced during the LSEM process.

25 137 *Table 1 LSEM process parameters used to produce the V44 alloy strips and the strain, strain rate,*  
26 138 *and temperature in the deformation zone during processing.*

$t_0$ (mm)	$t_c$ (mm)	$\lambda$	$\alpha$	$\gamma$	$\bar{\epsilon}$	$\Delta$ ( $\mu\text{m}$ )	$V$ (m/s)	$\dot{\epsilon}$ (1/s)	T (K)
0.1	0.33	3.3	0°	3.6	2.1	100	1.6	$3.1 \times 10^4$	1040

35 139 Impurity analysis of C, O, and N was performed on the as-cast coarse grain V44 and after LSEM  
36 140 processing by Luvak, inc. following ASTM E - 1019-24 (Oxygen & Nitrogen– Inert Gas Fusion  
37 141 and Carbon – Combustion Infrared Detection) standards. For the as-cast CG V44, 0.022 wt.% C,  
38 142 0.1 wt.% O, and 0.003 wt.% N was identified. After LSEM processing, the V44 possessed 0.017  
39 143 wt.% C, 0.047 wt.% O, and 0.006 wt.% of N.

## 42 144 2.2 Electron Microscopy Characterization

43 145 Microstructural characterization was performed using a JEOL JSM-IT800 Schottky Field  
44 146 Emission Scanning Electron Microscope (SEM) equipped with an Oxford Ultim Max 170 mm<sup>2</sup>  
45 147 energy dispersive X-ray spectroscopy (EDS) detector at a working distance of 10 mm and  
46 148 operating voltages ranging from 15 – 20 kV. Electron backscattered diffraction (EBSD) was  
47 149 performed using a step size of 1.07  $\mu\text{m}$ , 40 nm, and 15 nm for the EBSD maps at 300x, 5,000x,  
48 150 and 11,000x, respectively. After LSEM, the V44 was punched out into 3 mm diameter discs that  
49 151 were ground with 1200 and 2400 grit SiC paper to  $\sim 120$   $\mu\text{m}$  thickness. For SEM characterization,  
50 152 some of the 3 mm discs were polished with 6 and 3  $\mu\text{m}$  diamond paste polishing before being  
51 153 finished with a 80:20 solution of Struers OP-S and hydrogen peroxide. Following polishing,  
52 154 samples were sonicated in ethanol and dried under dry air. For transmission electron microscopy  
53 155 (TEM) characterization, some of the 3 mm discs were electropolished until perforation using a 4:1  
54 156 solution of methanol and sulfuric acid at -10 °C in a Struers Tenupol-5. TEM characterization was  
55 157 performed using the JEOL ARM 200CF AC and JEOL GrandARM 300CF AC-Scanning  
56 158 Transmission Electron Microscope (STEM). Sample thicknesses were taken from thickness maps

1  
2  
3  
4 159 using energy filtered transmission electron microscopy (EFTEM) utilizing an effective atomic  
5 160 number calculated for each specimen using the log-ratio technique [26].  
6

7 161 For the *in-situ* TEM heating experiment, a focused ion beam (FIB) equipped on a FEI Quanta dual-  
8 162 beam SEM/FIB was used to prepare a FIB liftout attached to a molybdenum TEM half grid. The  
9 163 lamella was capped with 3 protective layers: electron deposited Pt, ion deposited carbon, and ion  
10 164 deposited Pt. To finish the FIB lamella, both sides were polished with 5 kV, followed by 2 kV Ga  
11 165 ions for a minimum of 2 minutes. The *in-situ* TEM heating experiment was performed using a  
12 166 Gatan double tilt heating holder, heating the specimen from room temperature to 800 °C with a  
13 167 heating rate of 22 °/min. The vacuum of the TEM chamber was  $\sim 7 \times 10^{-6}$  Pa after 1 hour. The  
14 168 temperature was held at 800 °C for 30 minutes before cooling the specimen back to room  
15 169 temperature at the same rate as the heating.  
16  
17  
18

### 19 170 2.3 *In-situ* Dual-Beam Ion Irradiation

20 171 Samples were subjected to *in-situ* heating simultaneous dual-beam ion irradiation using 16 KeV  
21 172 He<sup>+</sup> and 1 MeV Kr<sup>2+</sup> ions at the Intermediate Voltage Electron Microscopy (IVEM) Facility at  
22 173 Argonne National Laboratory [27]. The sample chamber vacuum was  $\sim 7 \times 10^{-8}$  Torr. Specimens  
23 174 were heated to 700 °C over  $\sim 20$  minutes, after which the temperature was momentarily held  
24 175 constant before starting the dual-beam ion irradiation. Samples were subjected to fluxes of  
25 176  $9.3 \times 10^{12}$  ions $\cdot$ cm<sup>-2</sup>s<sup>-1</sup> and  $6.3 \times 10^{11}$  ions $\cdot$ cm<sup>-2</sup>s<sup>-1</sup> for He<sup>+</sup> and Kr<sup>2+</sup> ions, respectively, for 3,948 s  
26 177 (65 minutes and 48 seconds). This equates to fluences of  $3.67 \times 10^{16}$  ions $\cdot$ cm<sup>-2</sup> and  $2.47 \times 10^{15}$   
27 178 ions $\cdot$ cm<sup>-2</sup> for He<sup>+</sup> and Kr<sup>2+</sup> ions, respectively. In terms of dpa, this is expected to be equivalent to  
28 179  $\sim 5$  dpa with a He/dpa ratio of  $\sim 1$ .  
29  
30  
31

32 180 Damage calculations were performed using the Stopping Range of Ions in Matter (SRIM) 2013  
33 181 Pro with the Kinchin-Pease model, and results are shown in [Supplemental Figure S2](#) for the ternary  
34 182 and quaternary systems. Since all constituents of the alloy systems are transition metals, the value  
35 183 of 40 eV was set as the displacement energy for all the elements as suggested by Stoller *et al.* [28].  
36 184 The value of 40 eV was used in this work to compare and be consistent with other studies [29].  
37  
38

### 39 185 2.4 *Modeling and Simulations*

40 186 Metropolis Monte Carlo simulations with a cluster expansion (CE) Hamiltonian and density  
41 187 functional theory (DFT) on V<sub>92</sub>Cr<sub>4</sub>Ti<sub>4</sub> (at.%) were performed to gain a deeper understanding of the  
42 188 equilibrium states at different temperatures. The supercell contains 8192 atoms in the form of  
43 189  $16 \times 16 \times 16$  body-centered cubic (BCC) unit cells. The sample was first heated up to 2000 K and  
44 190 then cooled down to 200 K with a temperature decrement of 200 K. To reach equilibrium, we  
45 191 applied 4000 Monte Carlo steps per atom at each temperature, and after the system reached  
46 192 equilibrium, another 5000 Monte Carlo steps per atom were applied to calculate averages for data  
47 193 analysis.  
48  
49  
50

### 51 194 2.5 *Ex-situ* Nanoindentation

52 195 Nanoindentation was performed using a Bruker-Hysitron TI Premier I with a standard low load  
53 196 transducer capable of a max load of  $\sim 11$  mN. Indents were performed in open-loop displacement-  
54 197 controlled mode to a depth of 200 nm using a diamond Berkovich indenter. Both loading and  
55 198 unloading segments were performed with a strain rate of 0.05 s<sup>-1</sup>. A 10 s hold segment at the peak  
56 199 displacement was used to accommodate creep. Spacing between indents were 10  $\mu$ m. Hardness  
57 200 values were calculated using 95% of the peak load and an Oliver-Pharr fit for the tip area function.  
58  
59  
60  
61  
62  
63  
64  
65

For reporting the nanoindentation hardness of the irradiated electropolished 3mm disc of LSEM V44 at 700 °C, 5 by 10 arrays of indents with 20 μm spacing were performed at an arbitrary distance away from the perforation hole in the center of the disc (see [Supplementary Figure S5A](#)). Reported average values of hardness for the irradiated specimen used values after the 100 μm arbitrary distance away from the perforation hole, which is the point at which the hardness values began to stabilize ([Supplementary Figure S5B](#)).

### 3. Results

#### 3.1 Microstructure of LSEM V44

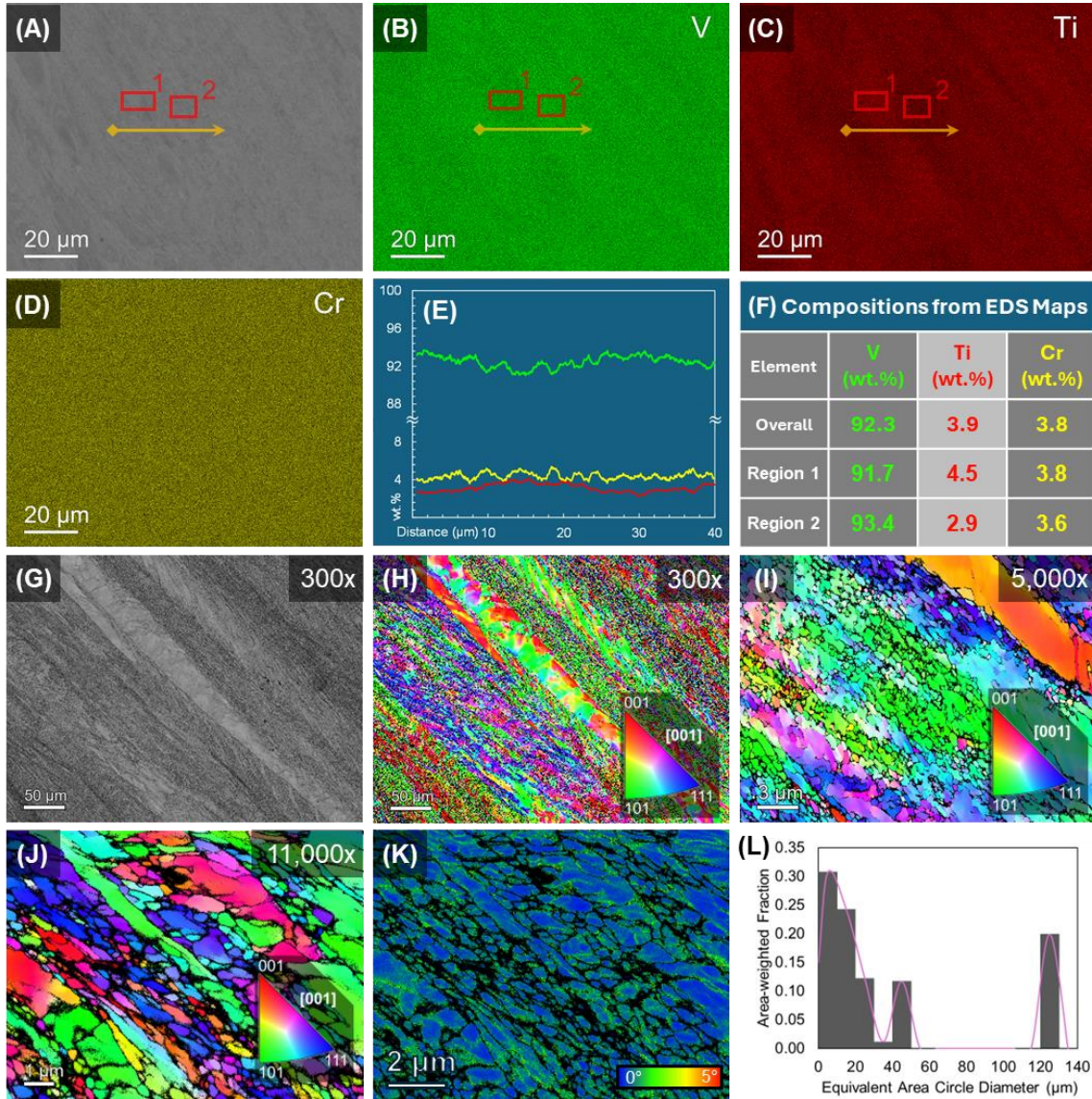


Figure 1: Backscattered SEM image of the LSEM V44 (A) with associated EDS maps for V (B), Ti (C), and Cr (D). A plot of the line scanned performed over the region indicated by the orange line in (A) is shown in (E). A table of the compositions is shown in (F) from the overall EDS map, as well as region 1 and region 2, as indicated by the red rectangles in (A), showing the variation in composition in and outside of one of the V-rich regions. Band contrast of the nanocrystalline V44 (G) with associated EBSD map (H). Higher magnification EBSD maps are shown, taken at 5,000x (I) and 11,000x (J). The kernel average misorientation map of the region in (K) is shown in (J). A plot of the weighted fraction of grains based on the equivalent area circle diameter of the region shown in (L).

The microstructure of the V44 after LSEM is shown in Figure 1. Overall, the EDS maps (Fig. 1B – D), show that the composition is homogeneously distributed with a composition of 92.3 wt.% V, 3.9 wt.% Ti, and 3.8 wt.% Cr (equivalent to  $V_{92.1}Ti_{4.1}Cr_{3.8}$  at.%). Diagonal streak-like regions can be observed in the V (Fig. 1B) and Ti (Fig. 1C) maps, regions with a slight enrichment in Ti (~0.4 at.%) and, consequently, depletion in V (see Figure 1B – C, 1F, region 1) as well as regions enriched in V (~1.7 at.%) and consequently depleted in Ti and Cr (see Figure 1B – C, 1F, region 2). A plot (Figure 1E) of the line scan (indicated by the orange arrow in Figure 1A – C) shows the compositional variation across the various enriched regions. The morphology of diagonal streak-like regions appears throughout the entire region and is suspected to be a result of the LSEM process.

Figure 1G shows a band contrast image with the associated EBSD map (Figure 1H) taken at a low magnification of 300x. The EBSD maps show an anisotropic grain microstructure with bands of elongated grains aligning with the diagonal streak-like regions observed in Figure 1A – C. Within the bands, the grains are not equiaxed and possess some level of texture. Higher magnification EBSD scans were performed at 5,000x (Fig. 1I) and 11,000x (Fig. 1J), highlighting the significant present of submicron grain sizes present in the sample after LSEM. The kernel average misorientation map (Fig. 1K) shows the presence of geometrically necessary dislocations present near a majority of the grain boundaries. This is to be expected with the as-processed LSEM specimen. Figure 1L shows the multi-modal grain size distribution of the system. While there is large fraction of fine grained ( $500 \text{ nm} < d < 5 \text{ }\mu\text{m}$ , where  $d$  is the equivalent area grain diameter), ultra-fine grained ( $100 < d < 500 \text{ nm}$ ), and nanocrystalline grains ( $d < 100 \text{ nm}$ ), there is still the presence of coarse grains above  $100 \text{ }\mu\text{m}$  in equivalent area diameter.

### 3.4 Ex-Situ Nanoindentation

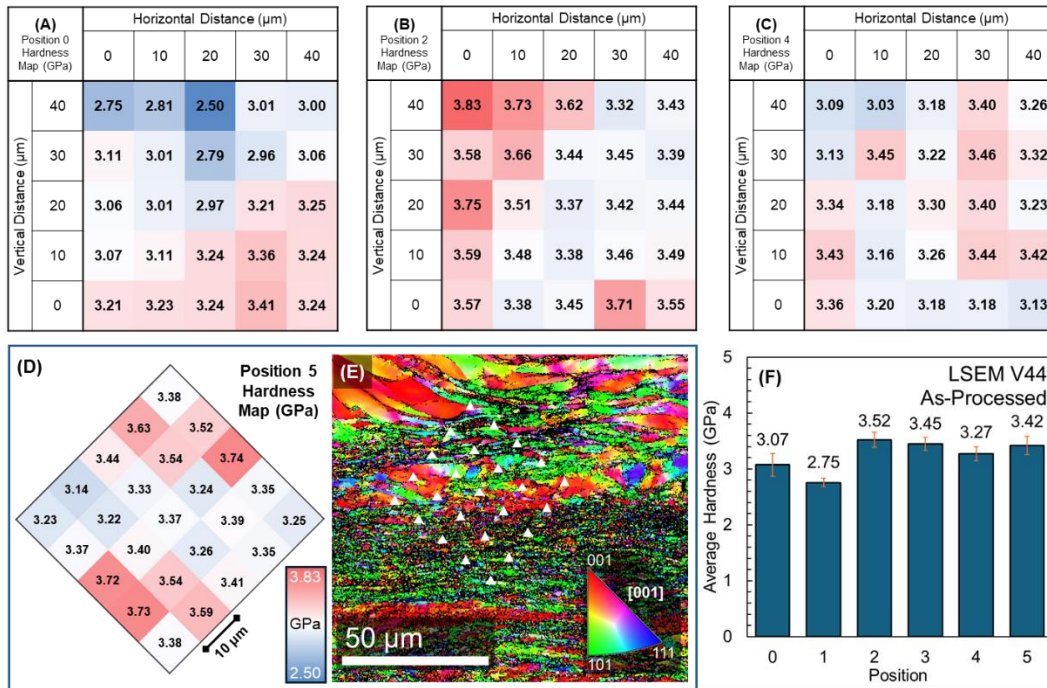


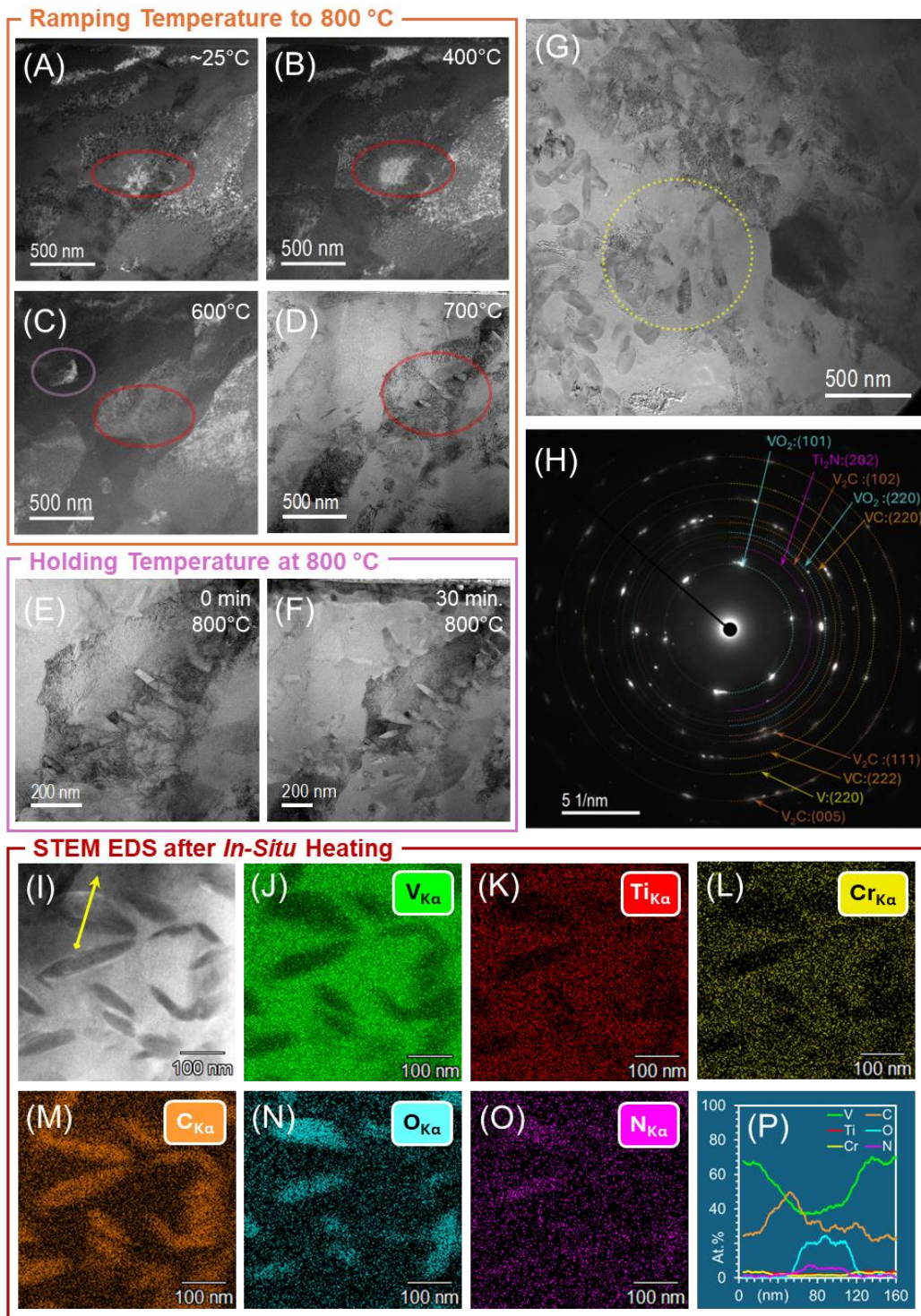
Figure 2: Nanoindentation maps of two arbitrary regions on the LSEM V44 specimen (A – C). Hardness map (D) associated with the region in the EBSD map shown in (E). Inset intensity bar in (D) represents the maximum and minimum values for all the nanoindentation positions, including the maps shown in (A – C). White triangles (not to scale; enlarged for emphasis) indicate

1  
2  
3  
4  
5  
6  
7  
8  
9  
10  
11  
12  
13  
14  
15  
16  
17  
18  
19  
20  
21  
22  
23  
24  
25  
26  
27  
28  
29  
30  
31  
32  
33  
34  
35  
36  
37  
38  
39  
40  
41  
42  
43  
44  
45  
46  
47  
48  
49  
50  
51  
52  
53  
54  
55  
56  
57  
58  
59  
60  
61  
62  
63  
64  
65

244 *the position of the indents in the EBSD map. (F) shows a plot of the average hardness with standard deviation of the different*  
245 *positions of the LSEM V44 specimen.*

246 Nanoindentation was performed in five different arbitrary regions on the LSEM V44 specimen.  
247 **Figure 2A – D** show hardness maps of three of the regions, showing a random spread of values.  
248 **Figure 2E** shows a post nanoindentation EBSD map of the indents indicated in **Figure 2D**. From  
249 the EBSD, some of the indents are expected to have fallen near or on the grain boundaries. Given  
250 the large presence of nanocrystalline and ultrafine sized grains, the values shown incorporate these  
251 microstructural features. The average hardness across each of the tested regions is shown in **Figure**  
252 **2F**. The variation of hardness in different regions is attributed to the heterogeneous microstructure  
253 with a multimodal grain size distribution. Indents from position 0 and 1 likely landed on coarser  
254 grains such as those observed in **Figure 1H**. For vanadium and many of its alloys, the Zener  
255 anisotropy ratio is near 1 [30]. Thus, any texture in the sample is not expected to lead to significant  
256 differences in the hardness, indicating the difference in hardness may be attributed to grain size  
257 with the presence of grain boundaries, as well as strain hardening from an increased number of  
258 dislocations produced by the LSEM process.

259 3.2 In-Situ TEM Heating



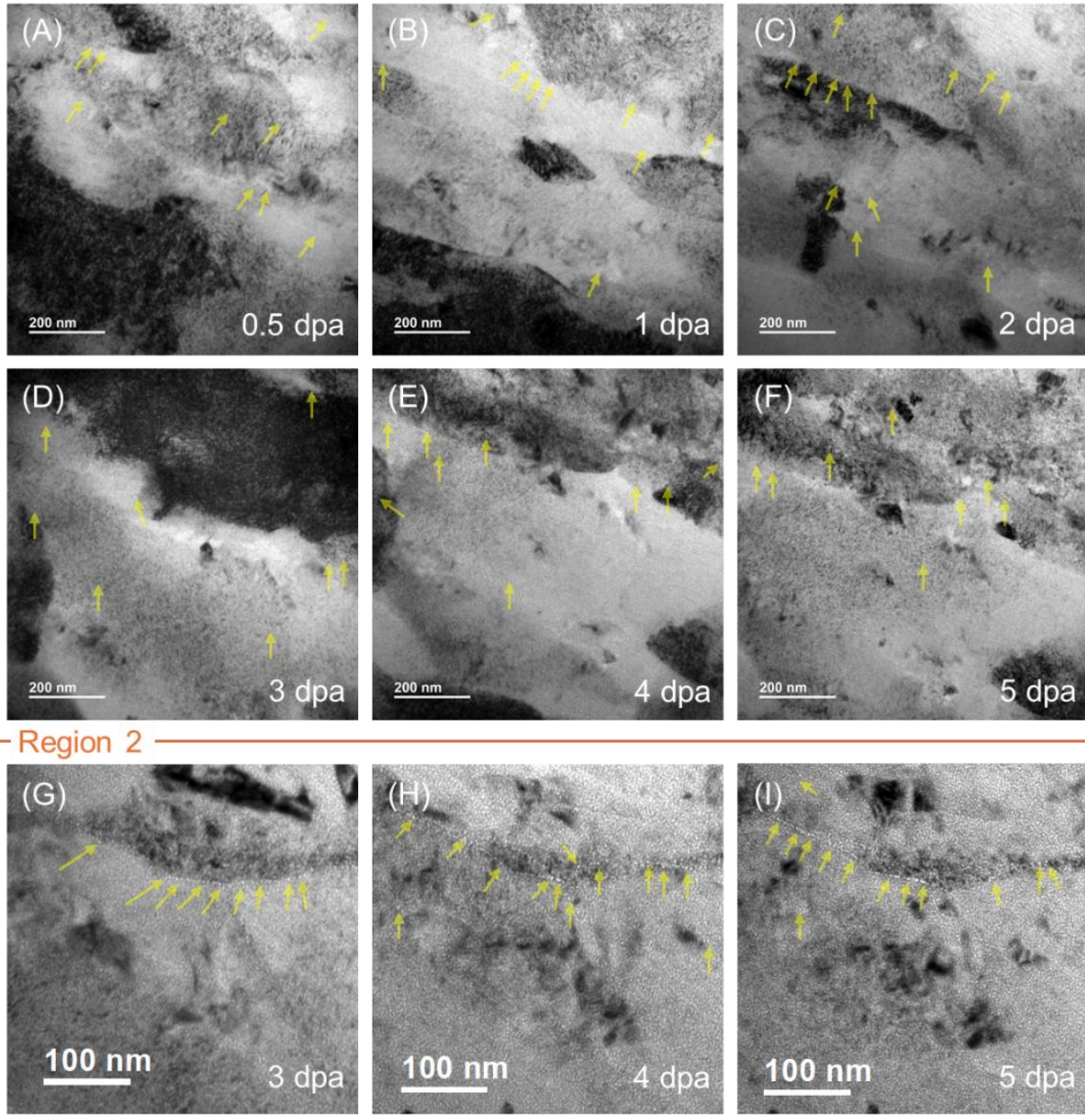
261 Figure 3: STEM-BF images of the LSEM V44 taken during the temperature ramp to 800 °C at room temperature (a), 400 °C (B),  
 262 600 °C (C), 700 °C (D). The red oval highlights a feature evolving with temperature. STEM-BF images were taken at 0 minutes  
 263 (E) and 30 minutes (F) at 800 °C. Brightfield TEM image (G) of the LSEM V44 after being exposed to 800 °C for 30 minutes with  
 264 associated SAD pattern (H) of the region highlighted by the yellow dashed circle in (G) STEM-ADF after annealing (I) with  
 265 associated EDS maps of V (J), Ti (K), Cr (L), C (M), O (N), and N (O). A plot of the line scan indicated by the yellow arrow in (I)  
 266 is shown in (P).

1  
2  
3  
4 267 To gain insight into the thermal stability of this specific grade of V44, in-situ TEM heating was  
5 268 performed on a TEM FIB liftout. Figure 3A – D shows scanning transmission electron microscope  
6 (STEM) bright field (BF) images taken without interrupting the temperature ramp at room  
7 269 temperature, 400 °C, 600 °C, and 700 °C. A red oval marks a feature that was being tracked and  
8 270 evolved during the temperature ramp. From Figure 3E – H, a larger condenser aperture was used  
9 271 to obtain better contrast in the images. Between 600 °C and 700 °C, plate-like features began to  
10 272 form (highlighted by the red oval in Fig. 3E). These features remained present at 800 °C and stable  
11 273 after 30 minutes at 800 °C. There was no significant change in microstructure of V44 observed  
12 274 during the 30-minute hold.  
13 275

14 276 More of the plate-like features can be observed in the BF-STEM image shown in Figure 3I.  
15 277 Associated EDS maps (Fig. 3J – M) from the region shows the presence of carbon in these features.  
16 278 A plot (Figure 3N) of the line scan over the area indicated by the yellow arrow in Figure 3I suggests  
17 279 that the feature is likely a vanadium carbide. The low value of vanadium measured in the line scan  
18 280 is likely skewed by the presence of carbon being detected throughout the chamber, especially after  
19 281 the in-situ heating in which dust and dirt present on the holder may have been burned off.  
20 282 Vanadium-oxide-rich precipitates can also be observed, separate from the vanadium carbide-rich  
21 283 precipitates. Their presence are further confirmed in the SAD shown in Figure 3H coming from  
22 284 the region in Figure 3G as indicated by the dashed yellow circle. The presence of Ti<sub>2</sub>N is also not  
23 285 surprising as they are predicted by the computed phased diagram of the composition shown in  
24 286 Figure 7B. Impurities such as carbon, oxygen, and nitrogen have been known to be difficult to  
25 287 eliminate and minimize in the production of V44 alloys [9, 10, 21], and have been observed to  
26 288 form Ti(C, O, N) and V(C, O, N) at elevated temperatures. From the impurity chemical analysis  
27 289 performed of the LSEM V44 specimen, there is 0.017 wt.% of C, 0.047 wt.% of O, and 0.006 wt.%  
28 290 of N present in the sample. Carbon burned off from the holder or from the protective carbon coating  
29 291 may serve as additional sources of carbon to form carbides during the *in-situ* TEM experiment.  
30  
31  
32  
33  
34  
35

36 292 From the in-situ TEM heating experiments, it was determined that this grade of V44 subjected to  
37 293 LSEM forms vanadium carbide after 600 °C. Up to 800 °C, some indications of recrystallization  
38 294 could be observed, however there was no significant grain coarsening occurring, despite the  
39 295 ultrafine and nanocrystalline grain sizes.  
40  
41  
42  
43  
44  
45  
46  
47  
48  
49  
50  
51  
52  
53  
54  
55  
56  
57  
58  
59  
60  
61  
62  
63  
64  
65

1  
2  
3  
4 296 3.3 Ion Irradiation



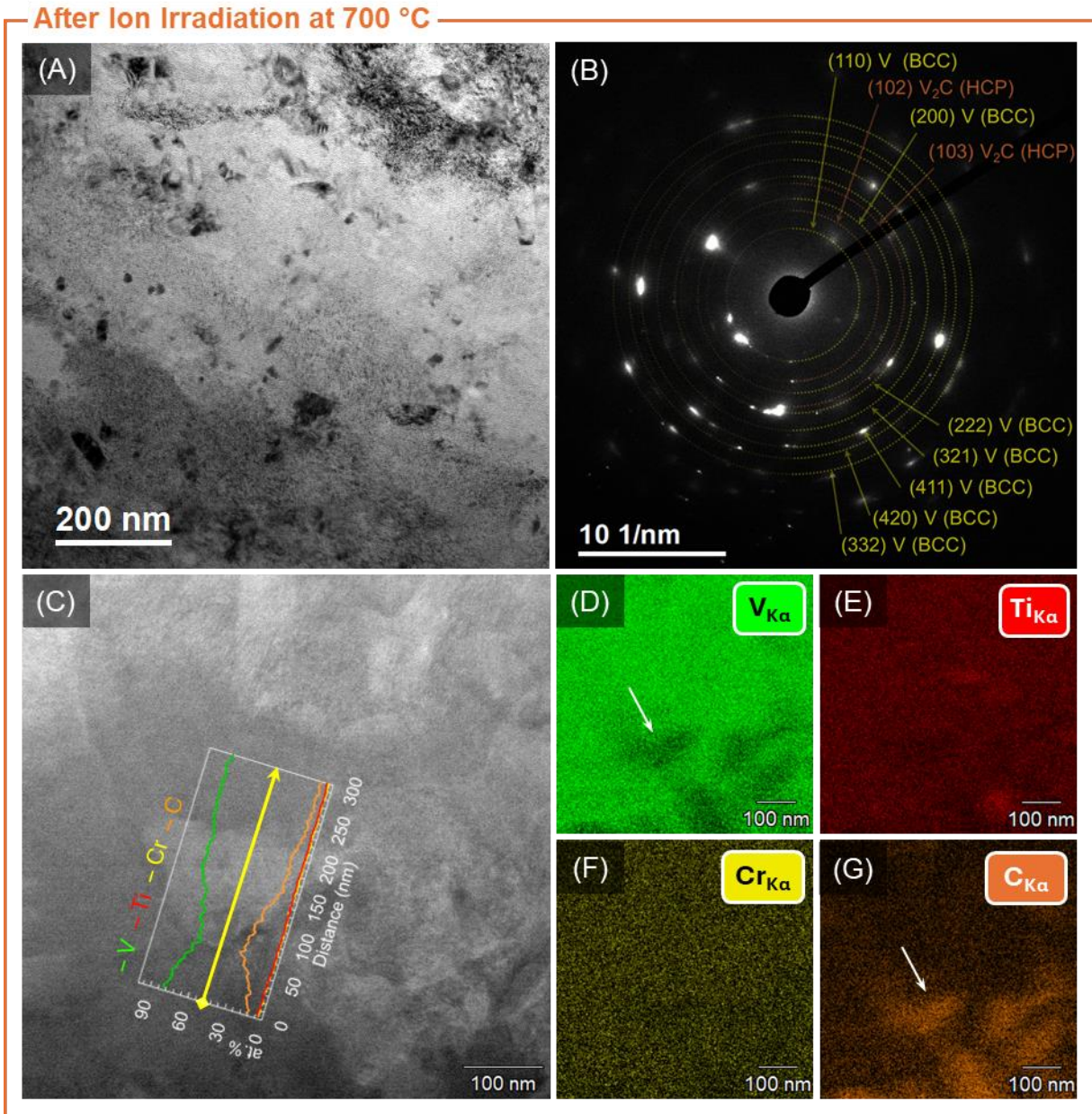
297  
298  
299  
300  
301  
302

Figure 4: Underfocused BF-TEM images taken during the in-situ dual-beam ion irradiation 700 °C at 0.5 (A), 1 (B), 2 (C), 3 (D), 4 (E), 4.5 (F) dpa to better visualize the presence of any He cavities in the sample. Underfocused BF-TEM images taken at a different region 2 taken at 3 (G), 4 (H), and 5 (I) dpa. Distinguishable He cavities are noted through the yellow arrows, though the ones highlighted do not represent all the He cavities observed in the images

303  
304  
305  
306  
307  
308

Dual beam ion irradiation of 16 KeV He<sup>+</sup> and 1 MeV Kr<sup>2+</sup> was performed at 700 °C, a temperature relevant for advanced nuclear reactor operations, while near the limit for the thermal stability of the multimodal V44. The ion irradiation was recorded and can be observed in [Supplemental Video 1](#). To capture the presence and quantify He cavities, underfocused BF-TEM images were taken to produce Fresnel fringe contrast that comes from the phase interference between the material matrix and the cavity interface [31]. Throughout the ion irradiation, there was dynamic formation, migration, and annihilation of defects in the material (see [Supplemental Video 1](#)). At 0.5 dpa (Fig.

4 309 4A), the presence of small He cavities can be observed, with the density of He cavities increasing  
 5 310 to 5 dpa. At 1 dpa (Fig. 4B), the small He cavities can be observed to cluster at grain boundaries  
 6 311 (see line of yellow arrows); however, they do not appear to grow significantly in size to 5 dpa (see  
 7 312 Figure 4F, 4I). While there is preferential clustering of cavities at the boundaries, cavities are also  
 8 313 seen well distributed throughout the grain matrices. There was no observable dynamic grain  
 9 314 growth or recrystallization occurring during the ion irradiation at 700 °C.



53 315  
 54 316 *Figure 5: Bright field TEM image with associated selected area diffraction pattern after dual-beam ion irradiation of 1 MeV Kr<sup>2+</sup>*  
 55 317 *and 16 KeV He<sup>+</sup> at 700 °C for ~1 hour (A and B). STEM-ADF taken the after the dual-beam ion irradiation at 700 °C (C) with*  
 56 318 *associated EDS maps of V (D), Ti (E), Cr (F), and C (G). A plot of the line scan indicated by the yellow arrow in (C) is overlaid.*  
 57 319 *White arrows point to vanadium carbide present in the sample after the ion irradiation.*

59 320 From the selected area electron diffraction (Fig. 5B) taken from a region in Figure 5A, most of the  
 60 321 diffraction spots correspond well with vanadium, with some spots matching well with vanadium

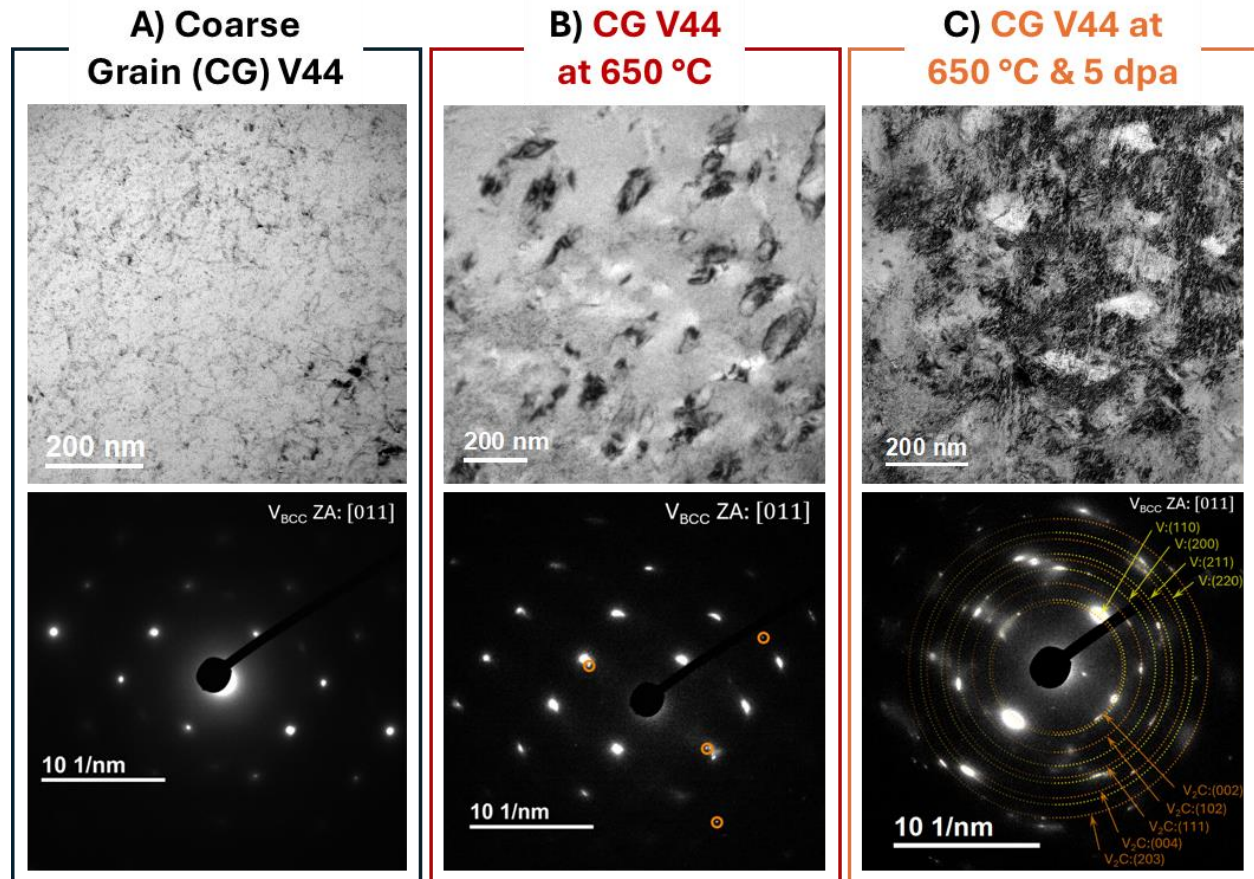


Figure 6: Brightfield TEM image of the as-cast coarse grain V44 with associated selected area diffraction along the [011] zone axis (A). BF-TEM image of the CG V44 after heating to the specimen to 650 °C with its associated SAD pattern (B). Spots in between and off the corners of the main vanadium diffraction spots (highlighted by the orange circles) can be observed, corresponding to vanadium carbides. BF-TEM image of the CG at 650 °C after dual-beam ion irradiation to 5 dpa with an associated SAD pattern. More diffraction spots can be observed, with many corresponding to  $V_2C$ . Orange arrows and dashed orange outlines point to and highlight a few of the vanadium carbides.

To better understand the ion irradiation response of the LSEM V44, the as-cast coarse grain V44 specimens were subjected to the same dual-beam ion irradiation conditions as the LSEM V44, but at a lower temperature of 650 °C. During the in-situ temperature ramp to the elevated temperature, the coarse grain V44 began exhibiting significant microstructural changes with the formation of carbides (see Figure 6A – 6B). The system was allowed time to briefly stabilize prior to being subjected to the dual-beam ion irradiation. The heavily defected microstructure after the ion irradiation is shown in Figure 6C. From the SAD taken after reaching 650 °C (Fig. 6B, bottom), but prior to the start of the ion irradiation, diffraction spots corresponding to vanadium carbides are observed, highlighted by orange circles. The presence of vanadium carbides is also observed by the SAD taken after the ion irradiation (Figure 6C, bottom). Vanadium carbide formation was

also observed in the LSEM V44 after heating the specimen to 700 C, but prior to beginning the ion irradiation (see Supplemental Figure S4). The observation of vanadium carbide before and after ion irradiation suggests that its formation is thermally driven and not specifically formed as a result of the ion irradiation.

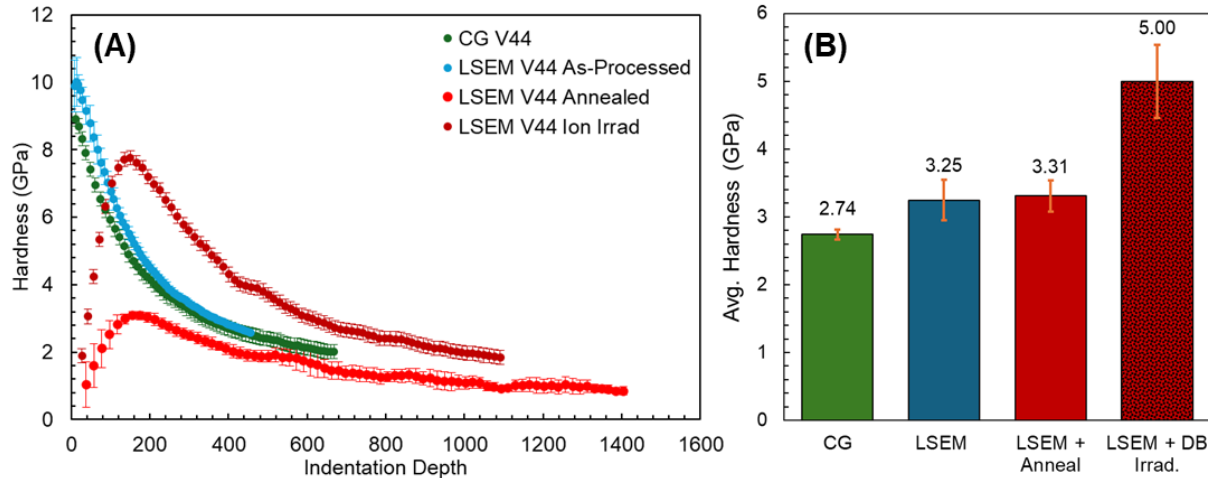


Figure 7: Plot of the instantaneous hardness with respect to depth of V44 calculated during the loading segment using nanoDMA in the as-cast coarse grain, as processed LSEM, LSEM subjected to 700 °C for 3,948s, and LSEM subjected to the dual-beam ion irradiation at 700 °C for 3,948s (A). Plot of the average hardness calculated from the unloading segment of V44 without nanoDMA in the as-cast coarse grain, as processed LSEM, LSEM subjected to 700 °C for 3,948s, and LSEM subjected to the dual-beam ion irradiation at 700 °C for 3,948s (B).

For insight on the irradiation hardening behavior of LSEM V44, Figure 7 compares the hardness of the coarse grain, LSEM, annealed LSEM at 700 °C, and dual-beam ion irradiated LSEM at 700 °C. Figure 7A shows the instantaneous hardness calculated as a function of depth using Bruker-Hysitron’s nanoDMA technique (a continuous stiffness measurement (CSM) function) applied to the loading segment. Due to the load limit of the system set up (10 mN), the hardness plots for the coarse grain and as-processed LSEM V44 do not completely stabilize. From Figure 7A, the ion irradiated LSEM V44 exhibits a higher hardness as compared to all the conditions, with the peak hardness for the dual-beam ion irradiated LSEM V44 corresponding well with the expected combined He<sup>+</sup> and Kr<sup>2+</sup> peak ion implantation (located ~160 nm) as simulated by SRIM (Supplemental Figure S2). Additionally, Figure 7B shows the average hardness of the different V44 conditions, calculated from the unloading segment of the indent without nanoDMA after reaching a peak depth of 200 nm. Compared to the hardness of the as cast coarse grain V44 (2.74±0.07 GPa), the as processed LSEM specimen has a higher average hardness (3.25±0.30 GPa). The increased hardness is expected considering the large fraction of nanocrystalline and ultrafine grain sizes and boundaries. As the sample possesses multimodal grain size distribution, it is not surprising for some indents to land on larger grains that possess a response similar to the coarse grain V44. The hardness does not significantly change after annealing the specimen at 700 °C for 3,948 s (3.31±0.23 GPa). The negligible change in hardness after heat treatment may be attributed to two competing mechanisms. As-processed LSEM produces a severely deformed microstructure (which can be observed by the EBSD maps shown in Figure 1E – G). Thus, when subjected to 700 °C for 3,948 s, dislocations, especially near the surface, are expected to anneal out, serving to soften the material with the reduced dislocation density. From the in-situ thermal investigations, there was no significant grain growth observed at these temperatures to suggest that

1  
2  
3  
4 378 softening is due to a Hall-Petch relationship in which large grain sizes lead to lower hardnesses.  
5 379 However, as observed in the in-situ heating experiments as well as previously observed in  
6 380 literature, carbon impurities form vanadium carbides which serve to precipitate strengthen the  
7 381 system. Thus, the competition between these two mechanisms is expected to play a major role in  
8 382 the negligible change in hardness of the annealed LSEM specimen. When subjected to dual-beam  
9 383 ion irradiation at 700 °C to a peak damage of ~5 dpa, the hardness increases to 5.00±0.54 GPa.  
10 384 Unlike in the annealed only specimen, when subjected to irradiation at elevated temperatures,  
11 385 additional defect production ion irradiation serves as another strengthening mechanism. For this  
12 386 reason, a significant increase in hardness is observed in the irradiated LSEM specimen at 700 °C.  
13  
14  
15  
16 387

## 17 18 388 **4. Discussion**

### 19 389 *4.1 Microstructure and Thermal Stability of Multimodal V44*

20 390 As a result of LSEM, the coarse grain structure of the as-cast V44 specimen (supplemental **figure**  
21 391 **S1A – B**) was significantly altered, forming a multimodal distribution of grains with  
22 392 nanocrystalline, ultrafine grained, and elongated coarse grains (**Figure 1E – G, I**). Unlike the  
23 393 elongated microstructure reported in other works [22], the elongated grains here are not continuous  
24 394 and, instead, are mostly broken up. This type of diverse grain morphology has been previously  
25 395 observed [24, 32, 33] as a result of LSEM processing of materials susceptible to adiabatic shear  
26 396 banding (ASB). ASB tends to happen in materials with lower thermal conductivity and higher heat  
27 397 capacity like V44 alloy. Higher strain rates and temperatures typical in machining operations  
28 398 promote formation of ASBs, which lead to the heterogenous microstructure. Strain localization  
29 399 within ASBs facilitates dynamic recrystallization and formation of ultrafine and equiaxed observed  
30 400 in figure 1G. Lower strains outside of ASBs result in the elongated coarse grains with subgrains  
31 401 (**Figure 1F**).  
32  
33  
34  
35

36 402 The increased number of grain boundaries from nanocrystalline and ultrafine grains serve as sinks  
37 403 for defects, thereby improving the radiation tolerance of the material [34-37]. In addition to aiding  
38 404 the radiation tolerance, the multimodal grain distribution is expected to also aid in improving the  
39 405 mechanical performance of the system. The presence of small grains has been shown to increase  
40 406 the strength of a material with the boundaries acting as barriers for dislocations to pile up and  
41 407 requiring increasing stress to nucleate further dislocations [38, 39]. Meanwhile, the presence of  
42 408 larger grains require more strain in order to form macrovoids for failure as well as more volume  
43 409 for dislocation slip to occur, thereby also improving the plasticity in the material [40-42].  
44 410 Multimodal grain morphologies incorporating nanocrystalline and ultrafine grain sizes have  
45 411 previously been observed to lead to enhanced strength and ductility in many other material systems  
46 412 such as Al [43, 44], Cu [45], Ti [46], Zr [41], and other compositionally complex alloys [40].  
47  
48  
49  
50  
51  
52  
53  
54  
55  
56  
57  
58  
59  
60  
61  
62  
63  
64  
65

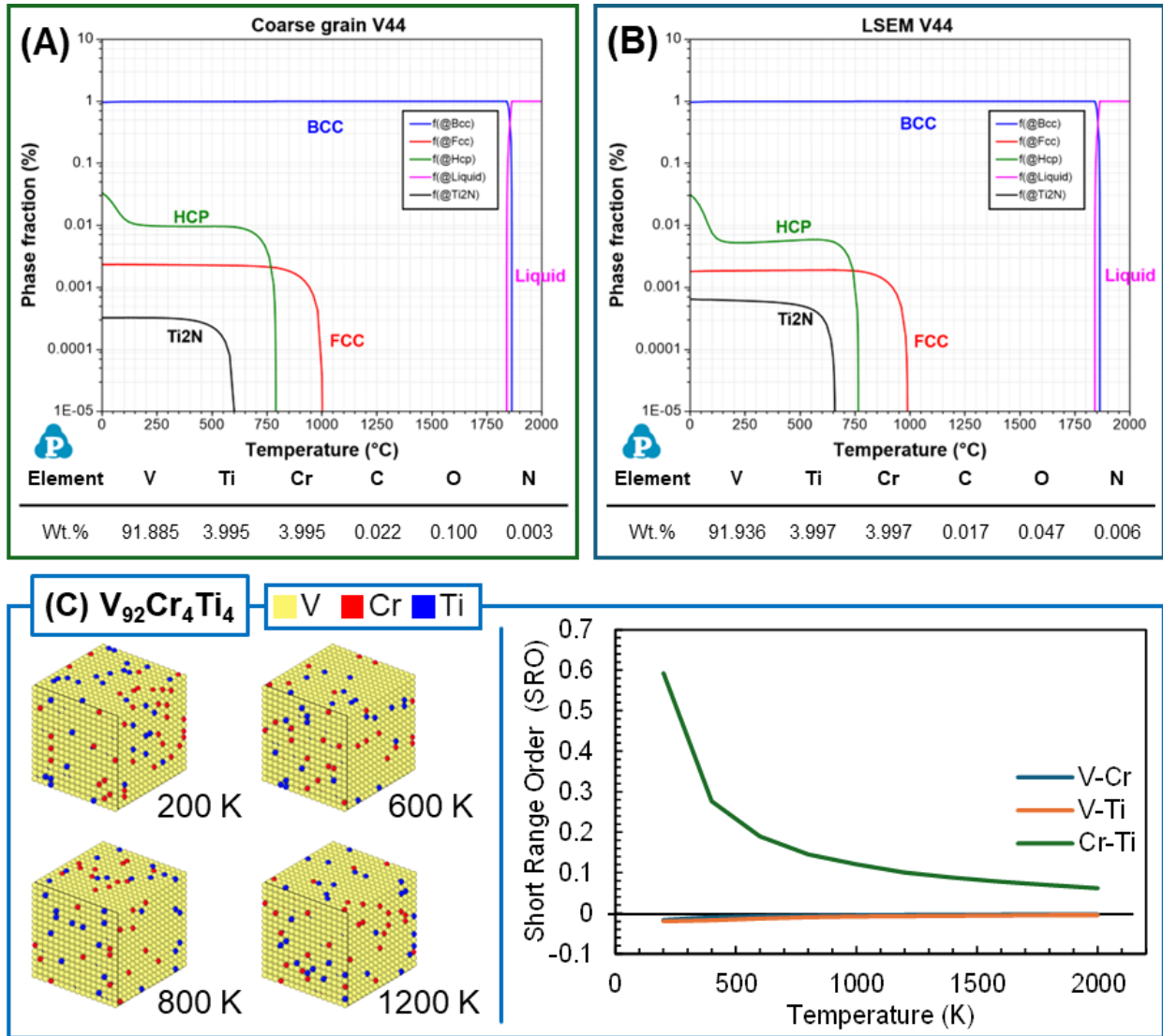


Figure 8: Phase diagram simulated using Pandat of V44 as-cast (A) and after LSEM processing (B) with a table of their respective compositions. The atomic configurations (left) from 200 K to 1200 K of V44 as well as the short-range ordering parameter with respect to temperature (right) using Monte Carlo (MC) modeling based on Density Functional Theory (DFT) and cluster expansion-Hamiltonian (CEH) are shown in (C).

To try to better understand the thermal stability of V44, phase diagrams were simulated using Pandat (see Figure 8A – B). At elevated temperatures, the general bulk phase is expected to correspond to BCC vanadium. This can be observed by the BCC vanadium spots observed in the selected area diffraction patterns for both the LSEM (see Figure 3H, Supplemental Figure S4B, Supplemental Figure 4B) and CG (see Figure 6B) V44. This is also in alignment with literature of simulated ternary phase diagrams V44 at the elevated temperatures  $\sim 700$  °C [47]. The next two largest phases expected are FCC and HCP phases, though both combined may amount to  $\sim 0.005$  phase fraction of the whole system. Among the more common vanadium carbides, VC possesses an FCC rock salt crystal structure and  $V_2C$  possesses a hexagonal crystal structure. From the SAD patterns observed in Figure 3H, Figure 5B and Figure 6B – C, there are diffraction spots (highlighted in orange) that match well with both of these carbides and crystal structures. Thus, the phase diagrams and the experimental phases observed in the TEM match well with the

1  
2  
3  
4 430 observation of impurity carbide phases forming at the elevated experimental temperatures of 650  
5 431 °C and 700 °C. The formation and presence of carbide phases may be favorable as they have been  
6 432 observed to improve the mechanical performance of V44 [6, 48], likely serving as obstacles for  
7 433 dislocation motion. In terms of radiation behavior, the additional interphase boundaries between  
8 434 the matrix and the carbide phases is expected to serve as sinks for defects [49].

9  
10  
11 435 In addition to simulating phase diagrams, Monte Carlo simulations based on density functional  
12 436 theory (DFT) and a Cluster Expansion-Hamiltonian (CEH) were performed to simulate and  
13 437 visualize the atomic configuration (plotted with the open visualization tool (OVITO)) of V44 at  
14 438 various temperatures (Figure 8B). These results match well with those performed by others in  
15 439 literature using finer temperature step sizes [50]. From the atomic configurations (Figure 8B, left),  
16 440 the system appears quite homogenized with the short range ordering (SRO) parameter [51]  
17 441 between the V – Ti and V – Cr binaries already near zero (Figure 8B, right). As the temperature  
18 442 increases to 800 K and further to 1200 K, there appears to be more intermixing between the Ti and  
19 443 Cr atoms, and indeed from plotting the short-range ordering parameter with respect to increasing  
20 444 temperature, there is less repulsion between Ti and Cr. Though, to start, the repulsive force between  
21 445 Ti and Cr was already low. These simulations suggest that at the elevated temperatures in the  
22 446 matrix and away from impurities, no compositional segregation is expected.

23  
24  
25  
26 447 Several groups have investigated different processing treatments of V44 to enhance its mechanical  
27 448 properties, especially at elevated temperatures. Tyumentsev et al. have investigated  
28 449 thermomechanical treatments involving a series of homogenization, aging, hydraulic compression,  
29 450 and multiple rolling cycles under various conditions, determining that the combination of  
30 451 heterophase nanostructuring and fine grained microstructure leads to increased high temperature  
31 452 strengths [12, 21]. Smirnov et al. also performed a series of thermomechanical treatments  
32 453 involving high temperature homogenization, extrusion, and multiple rolling cycles, but the final  
33 454 specimen was finished with vacuum annealing at different temperatures [22]. With increasing  
34 455 finishing annealing temperatures for 1 hour, the hardness of the specimen continuously dropped  
35 456 with a sharp decrease after 800 °C. At the same time, significant recrystallization and grain growth  
36 457 was observed at 800 °C. Ding et al. aged V-4Ti-4Cr at 800 °C, followed by room temperature  
37 458 reductions to different strain levels, and finishing with by annealing the specimen at 1100 °C for 1  
38 459 hour [11]. This treatment led to increased strengths in both the aged and cold-rolled specimen;  
39 460 however, the strength appears to be unstable under ion irradiation at elevated temperatures.  
40 461 Chernov et al. compared RAFM steels and V-4Ti-4Cr subjected to a traditional thermal treatment  
41 462 involving normalization and tempering and an additional special thermal cycling treatment [20].  
42 463 This treatment led to a homogeneous distribution of precipitates throughout the specimen which  
43 464 appeared to stably exist with the main BCC phase of the system. In all cases, elongated  
44 465 microstructures with large grains were observed, apart from those that were finished with a high  
45 466 temperature anneal above 800 °C.

46  
47  
48  
49  
50  
51 467 The work here also produced regions of elongated grain microstructure, as well as the presence of  
52 468 equiaxed ultrafine and nanocrystalline grains can also be observed within some of the ASB.  
53 469 Moreover, when exposed to the elevated temperatures of 800 °C for 30 minutes, the refined grain  
54 470 microstructure remained stable with negligible grain growth as observed by the in-situ TEM  
55 471 heating experiments. Negligible grain growth was also observed after the dual-beam ion irradiation  
56 472 that was performed at 700 °C for 3,948 s (65 minutes and 48 seconds). At elevated temperatures,  
57 473 only the formation of vanadium carbide was observed, consistent with findings reported in  
58 474 literature on the thermal stability of vanadium and its alloys. To better understand the origin of the  
59  
60  
61  
62  
63  
64  
65

1  
2  
3  
4 475 carbide precipitation occurring in this system, analysis of the C, O, and N impurities were  
5 476 performed on specimens before and after LSEM processing (see section 2.1). It was found that  
6 477 after LSEM processing, the impurity concentration of O and C decreased by 0.053 wt.% and 0.005  
7 478 wt.%, respectively. The reduction in impurity content as a result of mechanical deformation has  
8 479 been observed in stainless steels subjected to a tensile strain to failure in ultrahigh vacuum with  
9 480 outgassing of hydrocarbons [52, 53]. However, in the cited literature, outgassing of hydrocarbons  
10 481 is attributed to hydrocarbons adsorbed to the surface of the steel, which was released during the  
11 482 tensile strain and subsequent failure. Here, the C – O – N were present in the as-cast specimen and  
12 483 later decreased after the LSEM processing. It is suspected that for this system during the LSEM  
13 484 process, oxygen in solution of the as-cast V44, may be rapidly migrating to the newly formed grain  
14 485 boundaries prior to being released with the local elevated temperature. Thus, compared to other  
15 486 multi-step thermomechanical treatments, LSEM serves as a single step thermomechanical process  
16 487 to refine the grain microstructure of V44 with nanocrystalline and ultrafine grains, possessing  
17 488 comparable thermal stability as the unprocessed coarse grain V44.

#### 22 489 *4.2 Ion Irradiation Response of Multimodal V44 as compared to Coarse Grain and Literature*

23 490 In this work, multimodal V44 subjected to ion irradiation possesses notable irradiation tolerance  
24 491 with the presence of small He cavities that are well-dispersed throughout the grain matrix. The  
25 492 preferential clustering of He cavities at the grain boundaries was also observed, with minor  
26 493 observable coalescence of cavities at the boundaries given the temperatures and dose that the  
27 494 specimen was exposed to. The formation of small precipitates can be observed during the ion  
28 495 irradiation ([Supplemental Video S1](#)), however, compared to the coarse grain (CG) ion irradiation  
29 496 ([Supplemental Video S2](#)), the formation of these precipitates was not as prolific.

32 497 The observation of vanadium carbides after the ion irradiation at 700 °C, is expected as they have  
33 498 been previously observed in literature to be stable at similar conditions [48]. Their formation was  
34 499 also observed in the isolated *in-situ* TEM heating investigation discussed above, as well as in  
35 500 literature after elevated temperature ion irradiation, aging, and annealing investigations [9, 11, 21,  
36 501 54]. The elongated and plate-like shape, as well as the sizes are similar to those reported for  
37 502 vanadium and other alloys [55]. Since their presence was observed prior to the onset of the ion  
38 503 irradiation for both the LSEM ([Supplemental Figure S4](#)) as well as for the coarse grain ([Figure  
39 504 6B](#)) V44, the formation of vanadium carbides is suspected to be thermally driven, and not a result  
40 505 of ion irradiation. After being exposed to ion irradiation at elevated temperatures, the vanadium  
41 506 carbides remain stable and do not show signs of dissolution or a diffusion to form other carbides.

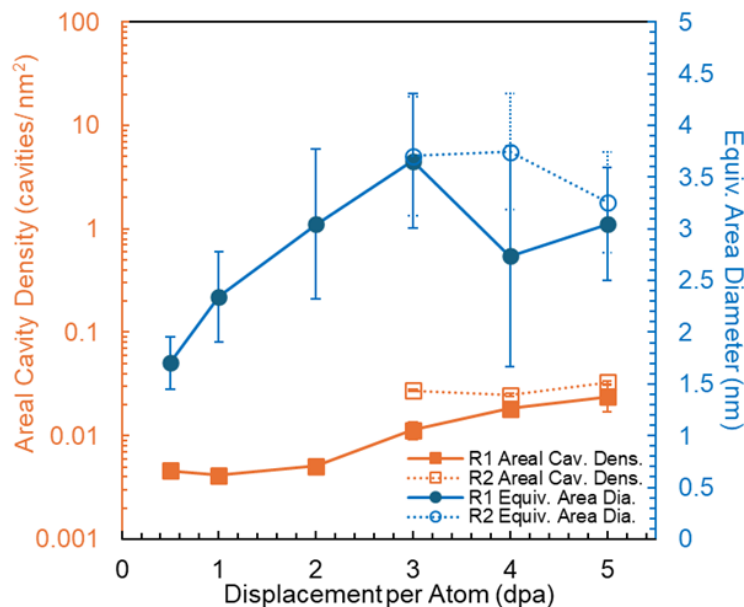


Figure 9: Plot of the He cavity analysis in terms of areal cavity density and equivalent area diameter with respect to dose (dpa) (A). From 3 dpa to 5 dpa, a second region began to be tracked (see figure 3G – I).

The overall areal cavity density and equivalent area diameter behavior of the multimodal V44 specimen with respect to dose is shown in Figure 9. With increasing dose, the areal cavity density increases to a value of  $0.024 \pm 0.007$  cavities/nm<sup>2</sup> at 5 dpa. In terms of the equivalent area diameter, there was an overall increase in the size to 3 dpa, peaking at  $3.7 \pm 0.6$  nm, followed by a drop in size to  $3.3 \pm 0.5$  nm at 5 dpa. The calculated swelling at 5 dpa for the multimodal V44 based on the average number of cavities, their average size, and the thickness measurement determined by EFTEM is 0.236%. To better qualify these results, the same dual-beam ion irradiation of 1 MeV Kr<sup>2+</sup> and 16 KeV He<sup>+</sup> was performed on coarse grain V44 (see Figure 6), though the irradiation occurred at 650 °C, as opposed to the 700 °C which was used for the LSEM V44 specimen. From Figure 6B, the formation of vanadium carbides can be observed from both the BF-TEM image as well as the associated SAD pattern of the CG V44, with orange circles highlighting the additional diffraction spots corresponding to vanadium carbides. To minimize the further formation of vanadium carbide, the ion irradiation was conducted at 650 °C. The final microstructure after the elevated temperature dual-beam ion irradiation is shown in Figure 6C. In multiple regions, there are heavily defected regions throughout the CG V44 grain matrix. The presence of vanadium carbides persists, as evidenced by the diffraction pattern. There is also the broadening of the diffraction spots which have been previously observed in ion irradiation to be an indicator of a damaged and defected lattice structure. Cavity analysis of the CG V44 after the dual-beam ion irradiation at 650 °C, reveal an areal cavity density of  $0.020 \pm 0.001$  cavities/nm<sup>2</sup> with an equivalent area diameter of  $4.3 \pm 0.7$  nm.

Compared to the coarse grain, the average equivalent area diameter of cavities in the LSEM V44 is lower, however the standard deviations between the two overlaps, suggesting a small improvement in ion irradiation tolerance. With respect to the areal cavity diameter, the LSEM possesses a slightly higher areal density as compared to the CG V44, however the standard deviations also overlap. It is likely that small cavities coalesced in the CG V44, leading to a lower overall areal density of cavities as compared to the LSEM specimen. As mentioned previously,

irradiation studies of grain refined materials have generally observed improvements in irradiation tolerance, generally attributed to the increased number of grain boundaries serving as efficient interstitial sinks which annihilate with vacancies near the grain boundary [56]. However, despite the significant increase in grain boundaries and interfaces in this work, the improvement in ion irradiation is negligible. This may be suggesting that the grain matrix plays a more dominant role as compared to the grain boundaries in V44 systems. This behavior has been previously observed in other alloys, notably in compositionally complex alloys (CCA) [57]. For nanocrystalline W-Ta-Cr-V, the rough energy landscape and high migration energy barrier of the grain matrix impeded the migration of He vacancy complexes to the grain boundaries, thereby slowing their coalescence at the grain boundary. A similar response can be observed in the LSEM V-4Cr-4Ti, though the onset of clustering can be observed after 3 dpa of the dual-beam ion irradiation. This is expected considering V44 is not as compositionally complex as the W-Ta-Cr-V system, meaning the migration energy barrier for the He vacancy complex may not be as high. Future simulations and calculations on the formation and migration energy of He vacancy complexes are required to better understand and validate the behavior observed in this work.

Regarding the the precipitates observed in **Figure 6B – C**, it is reasonable to assume from the SAD that some correspond to vanadium carbides, with their sizes being ~200 nm; this is larger than those observed in the LSEM V44 which are ~100 nm in terms of the longest diameter. Due to the sever plastic deformation, the LSEM V44 is expected to possess a larger number of dislocation cores as compared to the CG V44. Between the carbon – dislocation interaction, there can be attractive forces. Thus, if there are a wider spread and a larger number of dislocation cores in the specimen due to the LSEM process, this may lead to a homogenous distribution of carbon within the system. With the complex strain fields associated with the large number of dislocations and grain boundaries, this may serve to slow the kinetics for the formation and growth of these precipitates leading to the observed smaller carbide sizes in the LSEM V44. From the TEM images and *in-situ* TEM videos (**Supplemental Video 1 and 2**) there is also a noticeable difference in the presence of point defects and damage evolution which were prolific and longstanding in the coarse grain V44 as compared to the multimodal LSEM V44. These all suggest improvements in the ion irradiation behavior as a result of the LSEM process in V44.

Table 2: Summary of Ion Irradiation Nanoindentation on V-4Cr-4Ti

Description	Microstructure/ Grain Size	Irradiation Conditions	Irradiation Temperature	Peak dpa	Ion Irradiation Response	Hardness (GPa) Before Irradiation Conducted at RT	Hardness (GPa) After Irradiation Conducted at RT	Ref.
V-4Cr-4Ti (LSEM)	Multimodal with nanocrystalline and ultrafine grained (~45%*), and coarse grains (~55%*)	16 KeV He <sup>+</sup> and 1 MeV Kr <sup>2+</sup>	700 °C	~5	Cavity Equiv. Area Dia: 3.3±0.5 nm  Swelling: 0.236%	3.25±0.30	5.00±0.54	This Work
V-4Cr-4Ti (CG-Arc Cast)	>200 μm	16 KeV He <sup>+</sup> and 1 MeV Kr <sup>2+</sup>	650 °C	~5	Cavity Equiv. Area Dia: 4.3±0.7 nm	2.74±0.07	-	This Work

V-4Cr-4Ti (Zhang et al.)	~20 $\mu\text{m}$	30 KeV H <sup>+</sup> and 50 KeV He <sup>+</sup>	450 °C	0.18	-	3.68±0.30	5.05±0.37	[58]
V-4Cr-4Ti (Miyazawa et al.)	~20 – 30 $\mu\text{m}$	2.4 MeV Cu <sup>2+</sup>	200 °C	7.6	-	1.6	3.15	[59]
V-4Cr-4Ti (Luo et al.)	424 ± 124 $\mu\text{m}$	2.5 MeV Fe <sup>2+</sup>	550 °C	35	Cavity Dia: 3.1±0.4 nm Swelling: 0.02%	2.5	9.7	[60]
V-4Cr-4Ti (Fukumoto et al.)	~20 – 30 $\mu\text{m}$	2 MeV He <sup>+</sup>	500 °C	3.6	-	1.4	1.9	[61]
V-4Cr-4Ti (Ding et al.)	Coarse grains >10 $\mu\text{m}$	550 KeV Fe <sup>+</sup>	500 °C	20	Cavity Dia: 11.1±3.3 nm Swelling: -	-	-	[11]
V-4Cr-4Ti (Fukumoto et al.)	~20 – 30 $\mu\text{m}$	2 MeV He <sup>2+</sup>	500 °C	0.5	Cavity Dia: - Swelling: 0.4±0.03%	-	-	[62]
V-4Cr-4Ti (Fukumoto et al.)	~20 – 30 $\mu\text{m}$	2 MeV He <sup>2+</sup>	700 °C	0.5	Cavity Dia.:13.9±3.5 nm Swelling: 3.3±1.2%	-	-	[62]

\*Percentage represents the weighted area fraction of grains

When comparing the LSEM ion irradiation cavity numbers and sizes with literature (see Table 2), the observed values are higher. However, when comparing the size of cavities, the size reported here are significantly smaller with an upper limit of 3.3±0.5 nm. When exposed to 550 KeV Fe<sup>+</sup> ion irradiation to 20 dpa at 500 °C, cavities were observed to be 11.1±3.3 nm at the peak dose [11]. Others have irradiated V44 with 2 MeV He<sup>2+</sup> ions to 0.5 dpa at both 500 °C and 700 °C, observing cuboidal cavities at 700 °C that are 13.9±3.5 nm in size [62]. The values here are lower despite the higher dose (5 dpa) when compared to those reported by Fukumoto et al., who observed 0.4±0.03% swelling at 500 °C and 3.3±1.2% swelling at 700 °C for with 2 MeV He<sup>2+</sup> ions to 0.5 dpa [62]. Luo et. al. reported cavity sizes of 3.1±0.4 nm and swelling of 0.02% as a result of 2.5 MeV Fe<sup>2+</sup> at 550 °C to a peak of 35 dpa [60]. In terms of equivalent area diameter, the diameter of the multimodal V44 is observed to begin to stabilize at a size similar to that observed by Luo et al. The swelling of the multimodal LSEM V44 (0.236%) and number of cavities (0.024±0.007 cavities/nm<sup>2</sup>) is comparatively higher, though this discrepancy in number of cavities and presence of helium is attributed to the dual-beam ion irradiation of 1 MeV Kr<sup>2+</sup> and 16 KeV He<sup>+</sup> ion performed at 700 °C in this work.

Nanoindentation has been widely used to gain insight into the mechanical properties of V44, especially after irradiation. A few of these have been summarized in Table 2. Compared to most of

1  
2  
3  
4 583 the unirradiated V44 systems listed in the table, the LSEM V44 discussed in this work possesses  
5 584 a higher nanoindentation hardness, with the exception of Zhang et al. who reported a comparable  
6 585 hardness of  $3.68 \pm 0.30$  [58]. The comparable hardness observed by Zhang et al. may have been  
7 586 attributed to the presence of Ti-rich precipitates at the grain boundaries, which were not observed  
8 587 in the as-processed LSEM V44. The ion irradiated LSEM V44 performs comparably with most  
9 588 other V44 studied in literature, with comparable irradiation hardening as Zhang et al [58]. The  
10 589 irradiation hardening is not as high as what was observed by Luo et al. who reported a hardness of  
11 590 9.7 GPa, though in that work the sample was irradiated to a much higher dose of 35 dpa [60].

12  
13  
14  
15 591 It should be noted that many of the nanoindentation hardness values reported in literature were  
16 592 determined using continuous stiffness measurements (CSM) (or something similar) to plot  $H^2$   
17 593 versus  $1/h$ , where  $H$  is the instantaneous hardness at the respective depth,  $h$ , using the Nix-Gao  
18 594 model [63]. From this plot, a least square fit can be used to find the bulk, equivalent hardness  $H_0$ .  
19 595 The Nix-Gao model is often used as a technique for discerning and isolating indentation size  
20 596 effects and changes in the hardening slope of an indent due to the presence of an irradiation layer  
21 597 or different material near the surface of a material. However, Nix-Gao originally formulated the  
22 598 model based on the geometrically necessary dislocations present in single crystal or large grained  
23 599 systems. Similarly, many of the nanoindentation performed on irradiated V44 in literature (see  
24 600 [Table 2](#)) were performed on coarse grain specimens. With the Nix-Gao model, it becomes difficult  
25 601 to directly correlate changes in the hardening to a specific feature when there are multiple  
26 602 mechanisms (such as grain boundaries, precipitates, etc.) that may be observed as a function of the  
27 603 depth. For a multimodal grained specimen with a large fraction of nanocrystalline and ultrafine  
28 604 grains, multiple changes in the hardening slope can be observed in the as-processed specimen,  
29 605 making it challenging to interpret an appropriate bulk hardness ( $H_0$ ) from the as-processed  
30 606 specimen. The hardening curve from the loading segment is more complex after annealing the  
31 607 specimen at 700 °C, attributed to the formation of carbides. Moreover, ion irradiation adds another  
32 608 level of complexity in the interpretation of the hardening slope. As these factors should not be  
33 609 discounted, the values reported in [Figure 7B](#) serve as a simplified result, encompassing all these  
34 610 features. The hardness values in [Figure 7B](#) uses a simple load-unload indentation (without CSM),  
35 611 with the hardness,  $H$ , being calculated from the load at 95% of the unloading curve and a contact  
36 612 area determined by an Oliver-Pharr fit [64]. Although the indents performed in this study targeted  
37 613 a final depth of 200 nm, the total plastic zone and response of the indent will also incorporate part  
38 614 of the unirradiated LSEM V44 underneath the ion irradiation damage zone. This is expected to  
39 615 underestimate the real ion irradiation hardening observed between the annealed only LSEM V44  
40 616 and the dual-beam ion irradiated at 700 °C LSEM V44. Further controlled, targeted investigations  
41 617 are required to more accurately probe the hardening response associated with only the ion  
42 618 irradiation damage layer, as well as evaluate other mechanical properties (e.g. tensile, compression,  
43 619 and Vicker's Hardness) of LSEM V44 under extreme conditions.

## 50 51 620 **5. Summary**

52 621 This work showcases homogeneous V-4Cr-4Ti synthesized using arc melting which was  
53 622 successfully processed by large strain extrusion machining to produce a modified elongated  
54 623 multimodal microstructure composed of a majority of nanocrystalline and ultrafine grains. LSEM  
55 624 processing produces a severely plastically deformed microstructure with the presence of elongated  
56 625 grains and adiabatic shear bands. In terms of thermal stability, vanadium carbides began forming  
57 626 in the multimodal V44 after reaching 600 °C. Little grain growth was observed after reaching 800  
58 627 °C and holding the system at an elevated temperature for 30 minutes. After being exposed to dual-

1  
2  
3  
4 628 beam ion irradiation at 700 °C, He cavities can be observed throughout the system, though there  
5 629 is preferential clustering at the grain boundaries. Despite the clustering at the grain boundaries, the  
6 630 cavities exhibit little coalescence when exposed to ~5 dpa at 700 °C. There was a slight increase  
7 631 in the areal cavity density of cavities to ~ 5 dpa and the equivalent area diameter of cavities appear  
8 632 to have stabilized around 3 nm. Compared to the as-cast and unprocessed coarse grain V44 shown  
9 633 in this work, a lower number of other phases and precipitates were observed to have formed during  
10 634 the dual beam ion irradiation. In addition, a larger local area fraction of point defects from the ion  
11 635 irradiation remained in the CG V44 as compared to the LSEM V44 as observed from the *in-situ*  
12 636 ion irradiation videos. Nanoindentation reveals a ~50% increase in the hardness of the LSEM V44  
13 637 after the dual-beam ion irradiation at 700 °C. Further investigations are suggested to further  
14 638 quantify the mechanical capabilities and irradiation hardening mechanisms of LSEM V44.  
15 639 Ultimately, the LSEM V44 possesses similar ion irradiation response as what has been previously  
16 640 observed in literature. What is key to note is the grain stability of the LSEM V44 after ion  
17 641 irradiation. Negligible grain growth was observed at 700 °C, and despite the smaller grain size, the  
18 642 formation of precipitates and phases were slower than what was observed in the CG V44 which  
19 643 was ion irradiated at the lower temperature of 650 °C. Future work remains to understand the  
20 644 mechanical properties of multimodal V44 processed by LSEM and when subjected to extreme  
21 645 conditions such as temperature and irradiation. In addition, computational modeling and  
22 646 simulations of the formation and migration energies of defects will help to elucidate the underlying  
23 647 mechanisms of the ion irradiation response in vanadium-based alloys.

## 648 **CRedit Authorship**

649 **Skye Supakul:** Validation, Formal Analysis, Investigation, Methodology, Data Curation, Writing  
650 – Original Draft, Writing – Review & Editing, Visualization. **Ishtiaque Robin:** Validation,  
651 Investigation, Writing – Review & Editing. **Osman El-Atwani:** Conceptualization, Methodology,  
652 Resources, Data Curation, Writing – Review & Editing, Validation, Supervision, Visualization,  
653 Project Administration, Funding Acquisition. **Bochuan Sun:** Formal Analysis, Investigation,  
654 Writing – Original Draft, Writing – Review & Editing. **Enrique Martinez:** Methodology,  
655 Conceptualization, Validation, Writing – Review & Editing. **Dan Thoma:** Conceptualization,  
656 Methodology, Validation, Resources, Writing – Review & Editing. **Stuart Maloy:** Funding  
657 Acquisition, Resources, Writing – Review & Editing, Supervision, Project Administration. **Eda**  
658 **Aydogan:** Investigation, Validation, Supervision, Writing – Review & Editing. **Matthew Vigil:**  
659 Resources, Methodology, Writing – Original Draft, Writing – Review & Editing. **Kayla Yano:**  
660 Formal Analysis, Investigation, Writing – Review & Editing. **Damian Sobieraj:** Resources,  
661 Writing – Review & Editing. **Jan S. Wróbel:** Resources, Writing – Review & Editing. **Duc**  
662 **Nguyen-Manh:** Resources, Writing – Review & Editing. **Mert Efe:** Resources, Methodology,  
663 Writing – Original Draft, Writing – Review & Editing. **Wei-Ying Chen:** Resources, Investigation,  
664 Writing – Review & Editing.

## 665 **Declaration of Competing Interest**

666 The authors declare that they have no competing interests.

## 667 **Acknowledgments**

668 This work was supported by the U.S. Department of Energy, Advanced Research Projects Agency-  
669 Energy under contract DE-FOA-0003240, project number 84026A. This work was also supported  
670 by an Energy & Environment Directorate Mission Seed Laboratory Directed Research and  
671 Development (LDRD) project at Pacific Northwest National Laboratory. A portion of this research

1  
2  
3  
4 672 was performed on project award 61570 from the Environmental Molecular Sciences Laboratory, a  
5 673 DOE Office of Science User Facility sponsored by the Biological and Environmental Research  
6 674 program under Contract No. DE-AC05-76RL01830. This work was supported by the U.S.  
7 675 Department of Energy, Office of Nuclear Energy under DOE Idaho Operations Office Contract  
8 676 DE-AC07-05ID14517 as part of Nuclear Science User Facilities award #23-4744. The work at  
9 677 UKAEA was partially supported by the Broader Approach Phase II agreement under the PA of  
10 678 IFERC2-T2PA02. Views and opinions expressed were however those of the author(s) only and do  
11 679 not necessarily reflect those of the European Union or the European Commission. Neither the  
12 680 European Union nor the European Commission can be held responsible for them. D.N.M. also  
13 681 acknowledged funding by the EPSRC Energy Programme (grant number EP/W006839/1). This  
14 682 work was also completed with the help of Tim McAllister and Michael Blazon for their help in the  
15 683 LSEM processing and sample preparation, respectively.

### 684 **Data Availability**

685 All data needed to evaluate the conclusions in the paper are present in the paper and/or  
686 Supplementary Materials. Additional data related to this paper may be made available on request.

### 687 **References**

- 688 [1] G.J. Butterworth, Low activation structural materials for fusion, *Fusion Engineering and*  
689 *Design* 11(1) (1989) 231-244.
- 690 [2] E.E. Bloom, R.W. Conn, J.W. Davis, R.E. Gold, R. Little, K.R. Schultz, D.L. Smith, F.W.  
691 Wiffen, Low activation materials for fusion applications, *Journal of Nuclear Materials* 122(1)  
692 (1984) 17-26.
- 693 [3] R.H. Jones, H.L. Heinisch, K.A. McCarthy, Low activation materials, *Journal of Nuclear*  
694 *Materials* 271-272 (1999) 518-525.
- 695 [4] T. Muroga, J.M. Chen, V.M. Chernov, R.J. Kurtz, M. Le Flem, Present status of vanadium  
696 alloys for fusion applications, *Journal of Nuclear Materials* 455(1) (2014) 263-268.
- 697 [5] S.J. Zinkle, H. Matsui, D.L. Smith, A.F. Rowcliffe, E. van Osch, K. Abe, V.A. Kazakov,  
698 Research and development on vanadium alloys for fusion applications, *Journal of Nuclear*  
699 *Materials* 258-263 (1998) 205-214.
- 700 [6] T. Muroga, P.F. Zheng, Y. Yang, History, present status, and future directions of vanadium  
701 alloys for fusion reactors, *Current Opinion in Solid State and Materials Science* 36 (2025) 101224.
- 702 [7] D.L. Smith, B.A. Loomis, D.R. Diercks, Vanadium-base alloys for fusion reactor applications  
703 — a review, *Journal of Nuclear Materials* 135(2) (1985) 125-139.
- 704 [8] H.M. Chung, D.L. Smith, Tensile and impact properties of vanadium-base alloys irradiated at  
705 <430°C Work supported by the Office of Fusion Energy, US Department of Energy, under  
706 Contract W-31-109-Eng-38.1, *Journal of Nuclear Materials* 258-263 (1998) 1442-1450.
- 707 [9] T. Muroga, T. Nagasaka, K. Abe, V.M. Chernov, H. Matsui, D.L. Smith, Z.Y. Xu, S.J. Zinkle,  
708 Vanadium alloys – overview and recent results, *Journal of Nuclear Materials* 307-311 (2002) 547-  
709 554.
- 710 [10] D.R. Diercks, B.A. Loomis, Alloying and impurity effects in vanadium-base alloys, *Journal*  
711 *of Nuclear Materials* 141-143 (1986) 1117-1124.
- 712 [11] J. Ding, S. Yang, B. Zhu, Q. Li, Y. Long, F. Wan, Influence of high-temperature ion irradiation  
713 on microstructures of the deformed and heat-treated V-4Cr-4Ti alloy, *Fusion Engineering and*  
714 *Design* 125 (2017) 407-414.

- 1  
2  
3  
4 715 [12] A.N. Tyumentsev, I.A. Ditenberg, K.V. Grinyaev, V.M. Chernov, M.M. Potapenko, Multi-  
5 716 directional forge molding as a promising method of enhancement of mechanical properties of V-  
6 717 4Ti-4Cr alloys, *Journal of Nuclear Materials* 413(2) (2011) 103-106.  
7 718 [13] H. Watanabe, T. Muroga, T. Nagasaka, Effects of Irradiation Environment on V-4Cr-4Ti  
8 719 Alloys, *Plasma and Fusion Research* 12 (2017) 2405011-2405011.  
9 720 [14] R.W. Conn, Report of the DOE panel on low activation materials for fusion applications,  
10 721 United States, 1983.  
11 722 [15] C. Zhang, P. Zhang, R. Li, J. Zhao, C. Dong, Stability and migration of vacancy in V-4Cr-  
12 723 4Ti alloy: Effects of Al, Si, Y trace elements, *Journal of Nuclear Materials* 442(1) (2013) 370-376.  
13 724 [16] A. Impagnatiello, T. Toyama, E. Jimenez-Melero, Ti-rich precipitate evolution in vanadium-  
14 725 based alloys during annealing above 400 °C, *Journal of Nuclear Materials* 485 (2017) 122-128.  
15 726 [17] T. Furuno, H. Kurishita, T. Nagasaka, A. Nishimura, T. Muroga, T. Sakamoto, S. Kobayashi,  
16 727 K. Nakai, S. Matsuo, H. Arakawa, Effects of grain size on high temperature creep of fine grained,  
17 728 solution and dispersion hardened V-1.6Y-8W-0.8TiC, *Journal of Nuclear Materials* 417(1) (2011)  
18 729 299-302.  
19 730 [18] P.F. Zheng, J.M. Chen, T. Nagasaka, T. Muroga, J.J. Zhao, Z.Y. Xu, C.H. Li, H.Y. Fu, H. Chen,  
20 731 X.R. Duan, Effects of dispersion particle agents on the hardening of V-4Cr-4Ti alloys, *Journal of*  
21 732 *Nuclear Materials* 455(1) (2014) 669-675.  
22 733 [19] T. Nagasaka, T. Muroga, M. Imamura, S. Tomiyama, M. Sakata, Fabrication of High-Purity  
23 734 V-4CR-4TI Low Activation Alloy Products, *Fusion Technology* 39(2P2) (2001) 659-663.  
24 735 [20] V.M. Chernov, M.V. Leonteva-Smirnova, M.M. Potapenko, N.I. Budylnkin, Y.N. Devyatko,  
25 736 A.G. Ioltoukhovskiy, E.G. Mironova, A.K. Shikov, A.B. Sivak, G.N. Yermolaev, A.N.  
26 737 Kalashnikov, B.V. Kuteev, A.I. Blokhin, N.I. Loginov, V.A. Romanov, V.A. Belyakov, I.R. Kirillov,  
27 738 T.M. Bulanov, V.N. Golovanov, V.K. Shamardin, Y.S. Strebkov, A.N. Tyumentsev, B.K.  
28 739 Kardashev, O.V. Mishin, B.A. Vasiliev, Structural materials for fusion power reactors—the RF  
29 740 R&D activities, *Nuclear Fusion* 47(8) (2007) 839.  
30 741 [21] A.N. Tyumentsev, I.A. Ditenberg, K.V. Grinyaev, I.V. Smirnov, Y.P. Pinzhin, A.D. Korotaev,  
31 742 V.M. Chernov, M.M. Potapenko, M.V. Kravtsova, K.A. Moroz, N.A. Degtyarev, Microstructure  
32 743 and Mechanical Properties of Low-Activation V-4Ti-4Cr-(C, O, N) Vanadium Alloys Depending  
33 744 on Conditions of Their Technological and Thermomechanical Treatment, *Physics of Atomic*  
34 745 *Nuclei* 86(7) (2023) 1564-1576.  
35 746 [22] I.V. Smirnov, I.A. Ditenberg, K.V. Grinyaev, A.N. Tyumentsev, Y.P. Pinzhin, D.A. Osipov,  
36 747 Influence of the Annealing Temperature on the Grain Structure of V-4Ti-4Cr Alloy after  
37 748 Thermomechanical Treatment with Rolling, *Russian Physics Journal* 65(12) (2023) 2231-2237.  
38 749 [23] O. El-Atwani, J. Hinks, G. Greaves, S. Gonderman, T. Qiu, M. Efe, J.P. Allain, In-situ TEM  
39 750 observation of the response of ultrafine-and nanocrystalline-grained tungsten to extreme  
40 751 irradiation environments, *Scientific reports* 4 (2014) 4716.  
41 752 [24] M. Efe, O. El-Atwani, Y. Guo, D.R. Klenosky, Microstructure refinement of tungsten by  
42 753 surface deformation for irradiation damage resistance, *Scripta Materialia* 70 (2014) 31-34.  
43 754 [25] M. Efe, W. Moscoso, K.P. Trumble, W. Dale Compton, S. Chandrasekar, Mechanics of large  
44 755 strain extrusion machining and application to deformation processing of magnesium alloys, *Acta*  
45 756 *Materialia* 60(5) (2012) 2031-2042.  
46 757 [26] T. Malis, S.C. Cheng, R.F. Egerton, EELS log-ratio technique for specimen-thickness  
47 758 measurement in the TEM, *Journal of Electron Microscopy Technique* 8(2) (1988) 193-200.  
48 759 [27] M. Li, W.-Y. Chen, P.M. Baldo, In situ transmission electron microscopy with dual ion beam  
49 760 irradiation and implantation, *Materials Characterization* 173 (2021) 110905.  
50  
51  
52  
53  
54  
55  
56  
57  
58  
59  
60  
61  
62  
63  
64  
65

1  
2  
3  
4 761 [28] R.E. Stoller, M.B. Toloczko, G.S. Was, A.G. Certain, S. Dwaraknath, F.A. Garner, On the use  
5 762 of SRIM for computing radiation damage exposure, *Nuclear Instruments and Methods in Physics*  
6 763 *Research Section B: Beam Interactions with Materials and Atoms* 310 (2013) 75-80.  
7 764 [29] O. El-Atwani, H. Vo, N. Krienke, E. Martinez, J.K. Baldwin, W.-Y. Chen, M. Li, S. Fensin,  
8 765 Comparison of Dislocation Loop Formation Resistance in Nanocrystalline and Coarse-Grained  
9 766 Refractory High Entropy Alloys, *High Entropy Alloys & Materials* 1(2) (2023) 260-265.  
10 767 [30] X. Li, H. Zhang, S. Lu, W. Li, J. Zhao, B. Johansson, L. Vitos, Elastic properties of vanadium-  
11 768 based alloys from first-principles theory, *Physical Review B* 86(1) (2012) 014105.  
12 769 [31] J.V. Haag, M.J. Olszta, D.J. Edwards, W. Jiang, W. Setyawan, Visualization of Three-  
13 770 dimensional Helium Cavity Distribution in an Ion-irradiated Tungsten Heavy Alloy for Nuclear  
14 771 Fusion Materials, *Microscopy and Microanalysis* 29(Supplement\_1) (2023) 1565-1565.  
15 772 [32] Q. Wang, R.M. Shankar, Z. Liu, Y. Cheng, Crystallographic texture evolutions of Ti-6Al-4V  
16 773 chip foils in relation to strain path and high strain rate arising from large strain extrusion machining  
17 774 process, *Journal of Materials Processing Technology* 305 (2022) 117588.  
18 775 [33] S.L. Cai, L.H. Dai, Suppression of repeated adiabatic shear banding by dynamic large strain  
19 776 extrusion machining, *Journal of the Mechanics and Physics of Solids* 73 (2014) 84-102.  
20 777 [34] N. Nita, R. Schaeublin, M. Victoria, Impact of irradiation on the microstructure of  
21 778 nanocrystalline materials, *Journal of Nuclear Materials* 329-333 (2004) 953-957.  
22 779 [35] J.W. Yeh, S.K. Chen, S.J. Lin, J.Y. Gan, T.S. Chin, T.T. Shun, C.H. Tsau, S.Y. Chang,  
23 780 Nanostructured High-Entropy Alloys with Multiple Principal Elements: Novel Alloy Design  
24 781 Concepts and Outcomes, *Advanced Engineering Materials* 6(5) (2004) 299-303.  
25 782 [36] O. El-Atwani, J. Hinks, G. Greaves, J. Allain, S. Maloy, Grain size threshold for enhanced  
26 783 irradiation resistance in nanocrystalline and ultrafine tungsten, *Materials Research Letters* (2017)  
27 784 1-7.  
28 785 [37] Y. Zhang, M.A. Tunes, M.L. Crespillo, F. Zhang, W.L. Boldman, P.D. Rack, L. Jiang, C. Xu,  
29 786 G. Greaves, S.E. Donnelly, L. Wang, W.J. Weber, Thermal stability and irradiation response of  
30 787 nanocrystalline CoCrCuFeNi high-entropy alloy, *Nanotechnology* 30(29) (2019) 294004.  
31 788 [38] Y. Zou, H. Ma, R. Spolenak, Ultrastrong ductile and stable high-entropy alloys at small scales,  
32 789 *Nature Communications* 6(1) (2015) 7748.  
33 790 [39] Y.M. Wang, T. Voisin, J.T. McKeown, J. Ye, N.P. Calta, Z. Li, Z. Zeng, Y. Zhang, W. Chen,  
34 791 T.T. Roehling, Additively manufactured hierarchical stainless steels with high strength and  
35 792 ductility, *Nature materials* 17(1) (2018) 63-71.  
36 793 [40] B. Schuh, R. Pippan, A. Hohenwarter, Tailoring bimodal grain size structures in  
37 794 nanocrystalline compositionally complex alloys to improve ductility, *Materials Science and*  
38 795 *Engineering: A* 748 (2019) 379-385.  
39 796 [41] D. Guo, M. Li, Y. Shi, Z. Zhang, H. Zhang, X. Liu, B. Wei, X. Zhang, High strength and  
40 797 ductility in multimodal-structured Zr, *Materials & Design* 34 (2012) 275-278.  
41 798 [42] Y. Wang, M. Chen, F. Zhou, E. Ma, High tensile ductility in a nanostructured metal, *Nature*  
42 799 419(6910) (2002) 912-915.  
43 800 [43] S. Nelson, L. Ladani, T. Topping, E. Lavernia, Fatigue and monotonic loading crack  
44 801 nucleation and propagation in bimodal grain size aluminum alloy, *Acta Materialia* 59(9) (2011)  
45 802 3550-3570.  
46 803 [44] A. Magee, L. Ladani, T.D. Topping, E.J. Lavernia, Effects of tensile test parameters on the  
47 804 mechanical properties of a bimodal Al-Mg alloy, *Acta Materialia* 60(16) (2012) 5838-5849.  
48 805 [45] Y. Zhao, T. Topping, Y. Li, E.J. Lavernia, Strength and Ductility of Bi-Modal Cu, *Advanced*  
49 806 *Engineering Materials* 13(9) (2011) 865-871.  
50  
51  
52  
53  
54  
55  
56  
57  
58  
59  
60  
61  
62  
63  
64  
65

- 1  
2  
3  
4 807 [46] D.K. Yang, P.D. Hodgson, C.E. Wen, Simultaneously enhanced strength and ductility of  
5 808 titanium via multimodal grain structure, *Scripta Materialia* 63(9) (2010) 941-944.  
6 809 [47] J.Y. Lee, J.H. Kim, S.I. Park, H.M. Lee, Phase equilibrium of the Ti–Cr–V ternary system in  
7 810 the non-burning  $\beta$ -Ti alloy region, *Journal of Alloys and Compounds* 291(1) (1999) 229-238.  
8 811 [48] H. Takahashi, S. Ohnuki, T. Takeyama, H. Kayano, The effect of irradiation and post-  
9 812 irradiation annealing on the yield stress and microstructure of vanadium-carbon alloys, *Journal of*  
10 813 *Nuclear Materials* 96(3) (1981) 233-242.  
11 814 [49] Y. Zhao, P. Zheng, Y. Wei, H. Luo, W. Qian, G. Zhang, F. Li, M. Zhang, P. Zhang, Irradiation  
12 815 Hardening and Microstructure Study of MAX-Phase-Dispersion-Strengthened Vanadium Alloy  
13 816 under Self-Ion Irradiation, *Metals*, 2024.  
14 817 [50] T. Sparks, D. Nguyen-Manh, P. Zheng, J.S. Wróbel, D. Sobieraj, M. Gorley, T. Connolley, C.  
15 818 Reinhard, Y. Wang, B. Cai, Mechanical characterisation of V-4Cr-4Ti alloy: Tensile tests under  
16 819 high energy synchrotron diffraction, *Journal of Nuclear Materials* 569 (2022) 153911.  
17 820 [51] J.M. Cowley, X-Ray Measurement of Order in Single Crystals of Cu<sub>3</sub>Au, *Journal of Applied*  
18 821 *Physics* 21(1) (1950) 24-30.  
19 822 [52] Y. Ishikawa, T. Yoshimura, Mechanically stimulated outgassing from stainless steel surface,  
20 823 *Journal of Vacuum Science & Technology A* 9(3) (1991) 2021-2024.  
21 824 [53] P. Řepa, D. Orálek, Outgassing stimulated by deformation, *Vacuum* 53(1) (1999) 299-302.  
22 825 [54] H.Y. Chang, R.K. Viswanadham, C.A. Wert, Age-hardening in the V-C and Nb-C systems,  
23 826 *Metallurgical transactions* 5(8) (1974) 1907-1917.  
24 827 [55] D.R. Diercks, C.A. Wert, An electron microscopy study of carbide precipitation in vanadium,  
25 828 *Metallurgical Transactions* 3(7) (1972) 1699-1708.  
26 829 [56] Y.-Q. Chang, Q. Guo, J. Zhang, L. Chen, Y. Long, F.-R. Wan, Irradiation effects on  
27 830 nanocrystalline materials, *Frontiers of Materials Science* 7(2) (2013) 143-155.  
28 831 [57] O. El-Atwani, A. Alvarado, K. Unal, S. Fensin, J. Hinks, G. Greaves, J. Baldwin, S. Maloy,  
29 832 E. Martinez, Helium implantation damage resistance in nanocrystalline W-Ta-V-Cr high entropy  
30 833 alloys, *Materials Today Energy* 19 (2021) 100599.  
31 834 [58] Y. Zhang, R. Li, S. Diao, F. Wan, Q. Zhan, Plasticity improvement and radiation hardening  
32 835 reduction of Y doped V-4Cr-4Ti alloy, *Journal of Nuclear Materials* 560 (2022) 153508.  
33 836 [59] T. Miyazawa, T. Nagasaka, R. Kasada, Y. Hishinuma, T. Muroga, H. Watanabe, T. Yamamoto,  
34 837 S. Nogami, M. Hatakeyama, Evaluation of irradiation hardening of ion-irradiated V–4Cr–4Ti and  
35 838 V–4Cr–4Ti–0.15Y alloys by nanoindentation techniques, *Journal of Nuclear Materials* 455(1)  
36 839 (2014) 440-444.  
37 840 [60] H. Luo, F. Luo, Y. Chen, J. Wang, Q. Liu, F. Li, Z. Xie, W. Lin, L. Guo, Effect of yttrium  
38 841 content on microstructure and irradiation behavior of V-4Cr-4Ti-xY alloys, *Journal of Nuclear*  
39 842 *Materials* 559 (2022) 153480.  
40 843 [61] K.-i. Fukumoto, Y. Kitamura, S. Miura, K. Fujita, R. Ishigami, T. Nagasaka, Irradiation  
41 844 Hardening Behavior of He-Irradiated V–Cr–Ti Alloys with Low Ti Addition, *Quantum Beam*  
42 845 *Science*, 2021.  
43 846 [62] K.-i. Fukumoto, Y. Zou, T. Nagasaka, R. Ishigami, Microstructural changes and irradiation  
44 847 hardening behavior of V-4Cr-4Ti alloys irradiated with He ions using flash-electropolishing,  
45 848 *Journal of Nuclear Materials* 603 (2025) 155438.  
46 849 [63] W.D. Nix, H. Gao, Indentation size effects in crystalline materials: A law for strain gradient  
47 850 plasticity, *Journal of the Mechanics and Physics of Solids* 46(3) (1998) 411-425.  
48  
49  
50  
51  
52  
53  
54  
55  
56  
57  
58  
59  
60  
61  
62  
63  
64  
65

1  
2  
3  
4  
5  
6  
7  
8  
9  
10  
11  
12  
13  
14  
15  
16  
17  
18  
19  
20  
21  
22  
23  
24  
25  
26  
27  
28  
29  
30  
31  
32  
33  
34  
35  
36  
37  
38  
39  
40  
41  
42  
43  
44  
45  
46  
47  
48  
49  
50  
51  
52  
53  
54  
55  
56  
57  
58  
59  
60  
61  
62  
63  
64  
65

[64] W.C. Oliver, G.M. Pharr, An improved technique for determining hardness and elastic modulus using load and displacement sensing indentation experiments, Journal of Materials Research 7(6) (1992) 1564-1583.

854

1  
2  
3  
4  
5  
6  
7  
8  
9  
10  
11  
12  
13  
14  
15  
16  
17  
18  
19  
20  
21  
22  
23  
24  
25  
26  
27  
28  
29  
30  
31  
32  
33  
34  
35  
36  
37  
38  
39  
40  
41  
42  
43  
44  
45  
46  
47  
48  
49  
50  
51  
52  
53  
54  
55  
56  
57  
58  
59  
60  
61  
62  
63  
64  
65

Supplementary Materials for

## **Ion Irradiation Response of Multimodal V – 4Cr – 4Ti**

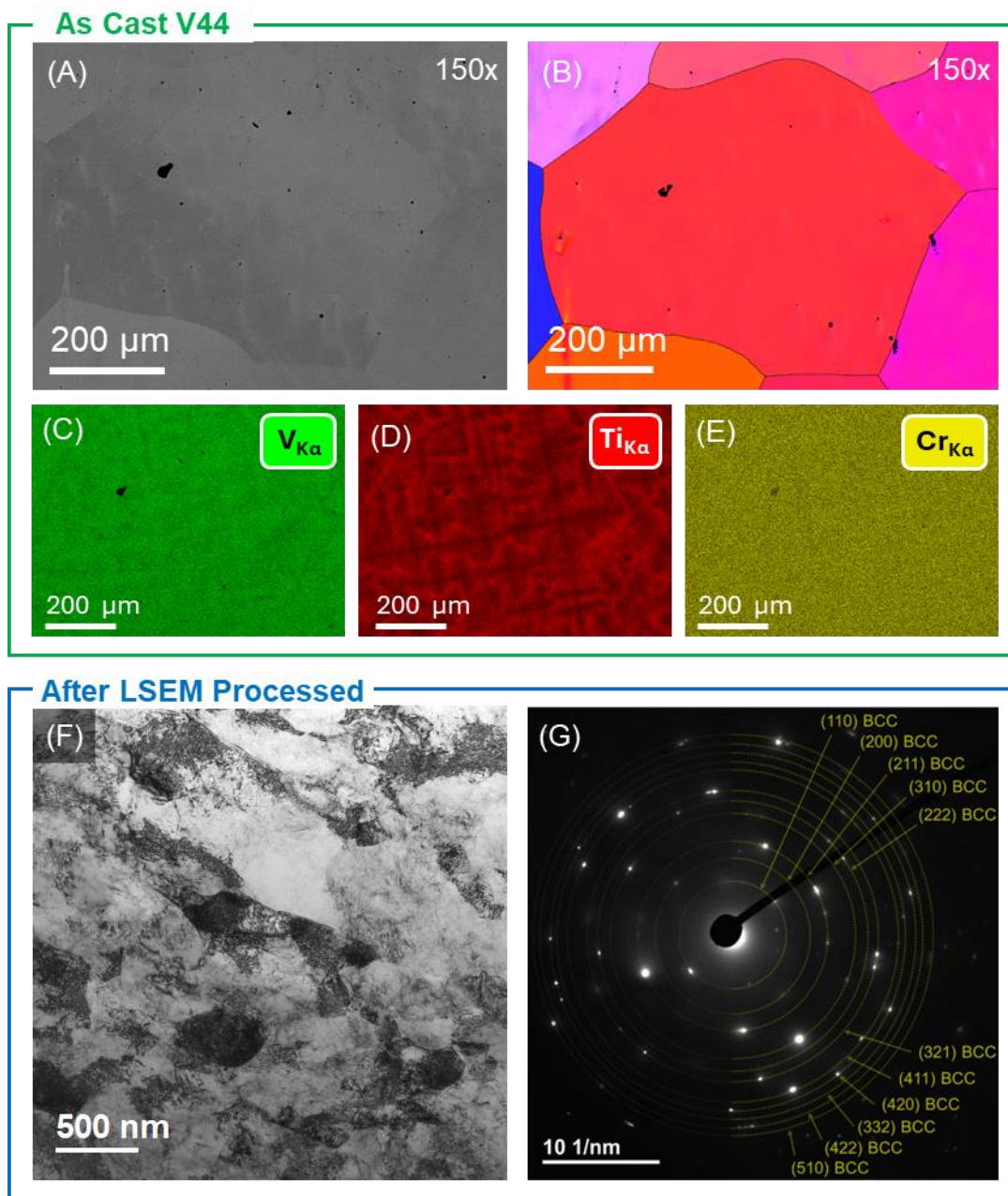
Skye Supakul *et al.*

\*Corresponding authors:

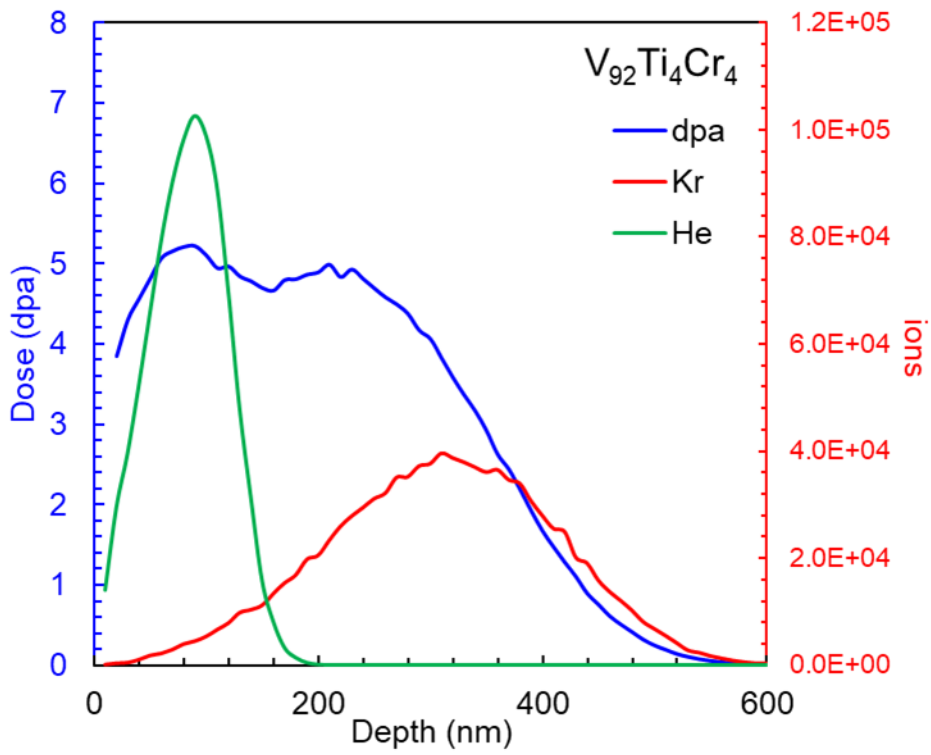
Skye Supakul ([skye.supakul@pnnl.gov](mailto:skye.supakul@pnnl.gov))

Osman El-Atwani ([osman.elatwani@pnnl.gov](mailto:osman.elatwani@pnnl.gov))

1  
2  
3  
4  
5  
6  
7  
8  
9  
10  
11  
12  
13  
14  
15  
16  
17  
18  
19  
20  
21  
22  
23  
24  
25  
26  
27  
28  
29  
30  
31  
32  
33  
34  
35  
36  
37  
38  
39  
40  
41  
42  
43  
44  
45  
46  
47  
48  
49  
50  
51  
52  
53  
54  
55  
56  
57  
58  
59  
60  
61  
62  
63  
64  
65

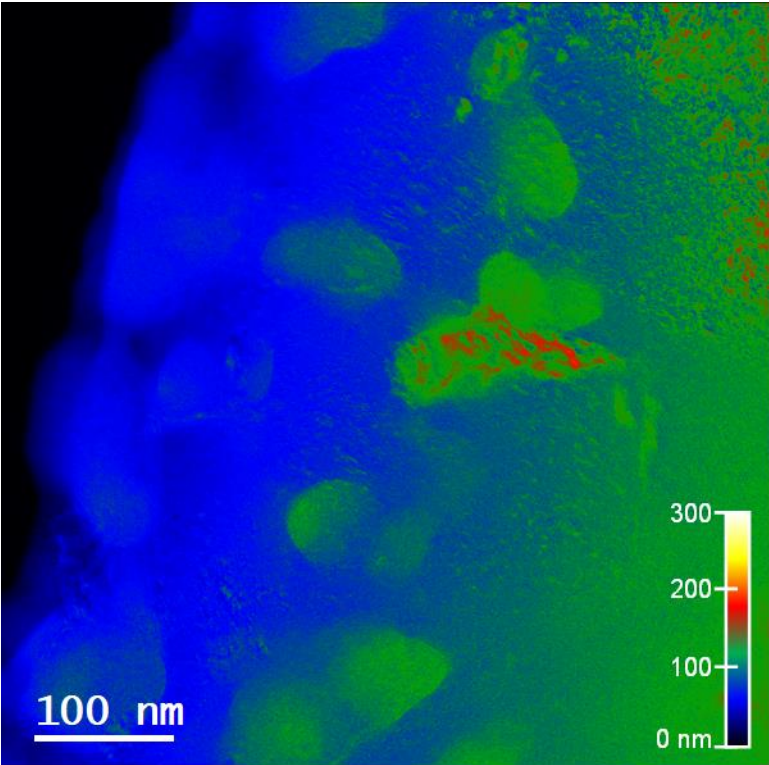


Supplemental Figure S1. Backscattered electron diffraction image of the as-cast coarse grain V44 (A) with an associated electron backscattered map of the grain orientation in the region (B) and energy dispersive electron X-ray spectroscopy maps of V (C), Ti (D), and Cr (E). Bright field TEM image with associated selected area diffraction pattern under the as processed condition (F and G).



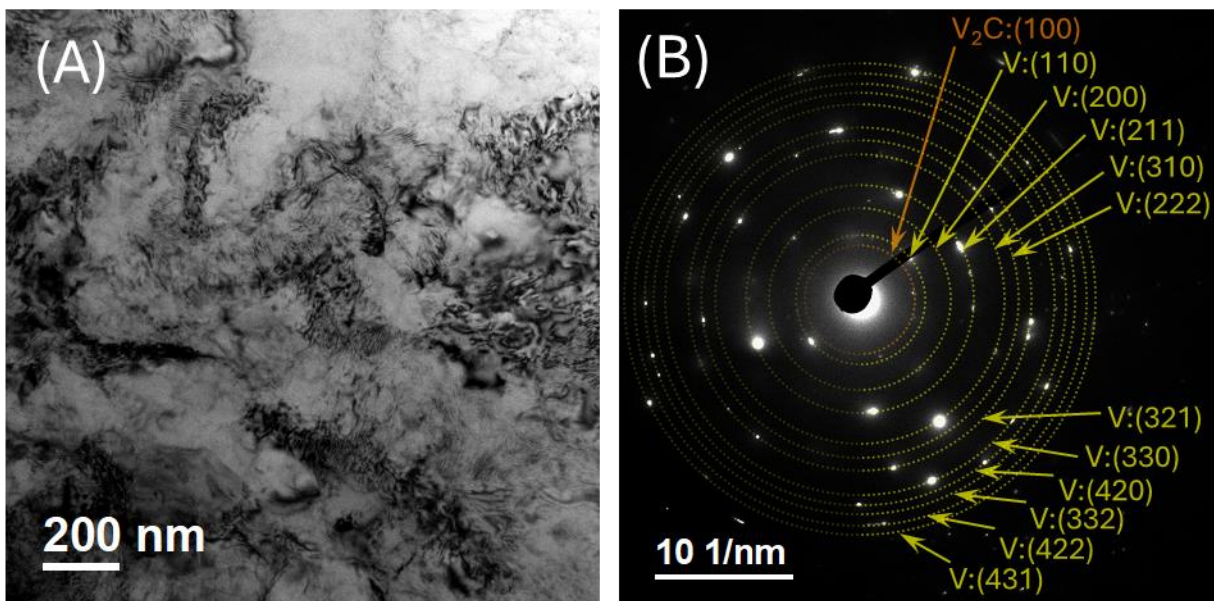
Supplemental Figure S2: Quick damage SRIM calculations using the Kinchin-Pease model for V-Ti-Cr

1  
2  
3  
4  
5  
6  
7  
8  
9  
10  
11  
12  
13  
14  
15  
16  
17  
18  
19  
20  
21  
22  
23  
24  
25  
26  
27  
28  
29  
30  
31  
32  
33  
34  
35  
36  
37  
38  
39  
40  
41  
42  
43  
44  
45  
46  
47  
48  
49  
50  
51  
52  
53  
54  
55  
56  
57  
58  
59  
60  
61  
62  
63  
64  
65

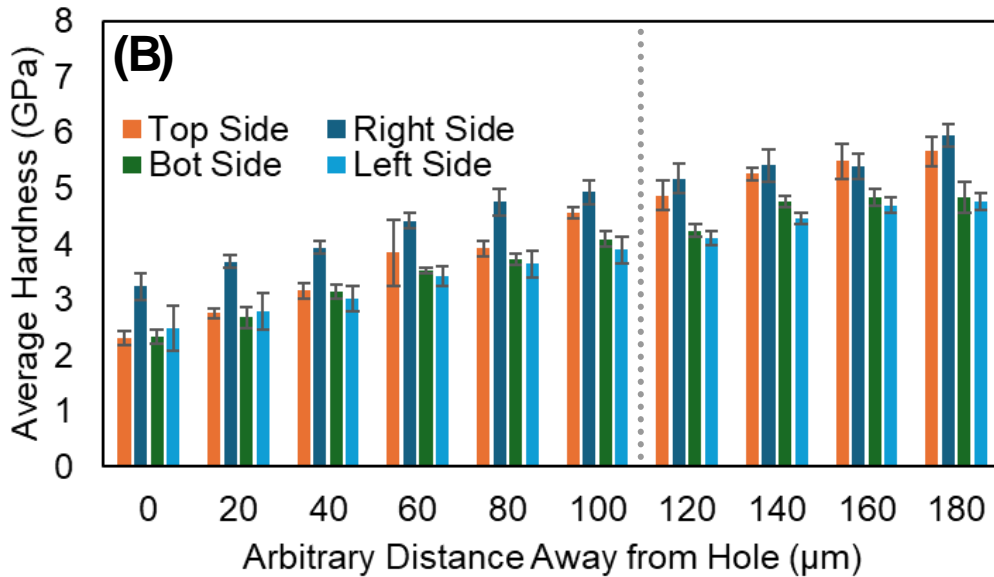
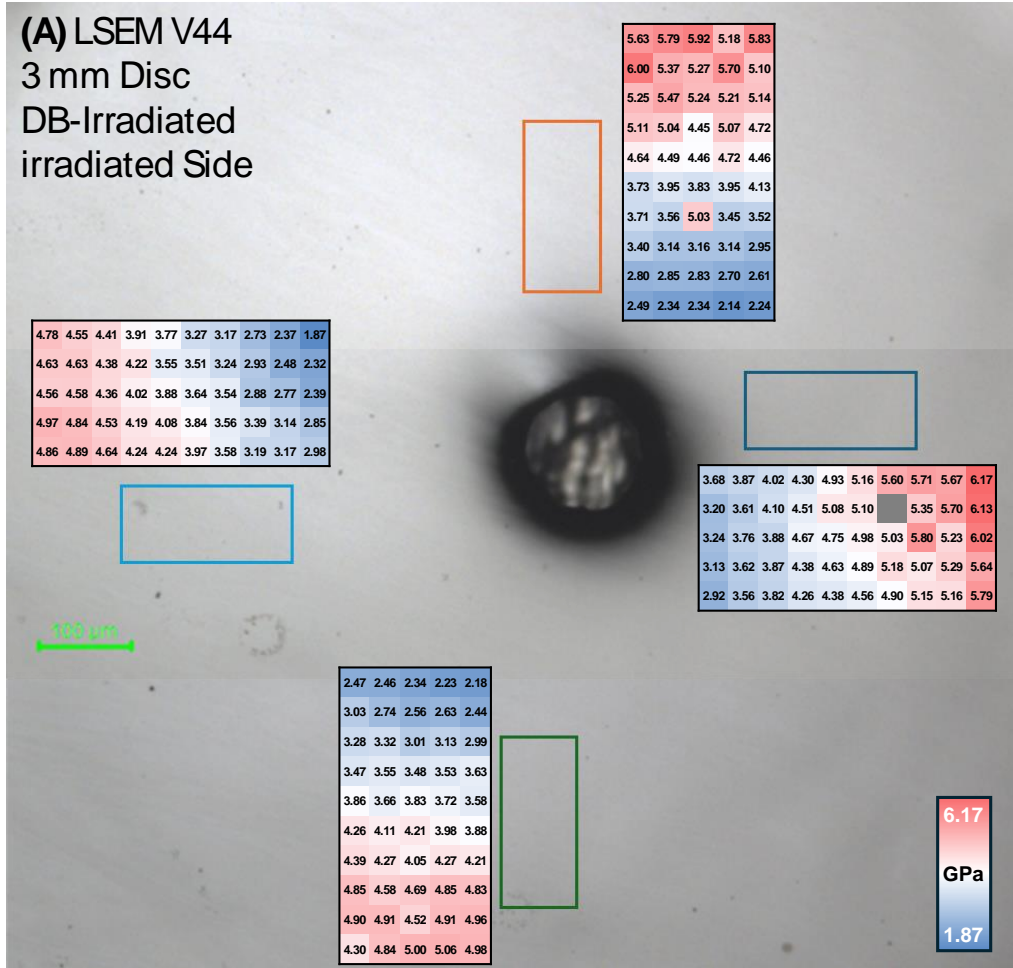


*Supplemental Figure S3: Thickness map of a region in the V-4Ti-4Cr taken after the dual-beam ion irradiation at 700 °C using energy filtered transmission electron microscopy (EFTEM).*

1  
2  
3  
4  
5  
6  
7  
8  
9  
10  
11  
12  
13  
14  
15  
16  
17  
18  
19  
20  
21  
22  
23  
24  
25  
26  
27  
28  
29  
30  
31  
32  
33  
34  
35  
36  
37  
38  
39  
40  
41  
42  
43  
44  
45  
46  
47  
48  
49  
50  
51  
52  
53  
54  
55  
56  
57  
58  
59  
60  
61  
62  
63  
64  
65



Supplemental Figure S4: Brightfield TEM image of the LSEM V44 (A) after being heated to 700 °C. The associated selected area diffraction is shown in (B), noting the spots for many different vanadium planes as well as the presence of some vanadium carbide.



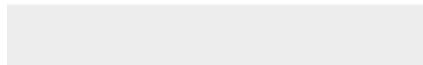
Supplemental Figure S5: Optical image of the 3mm disc of the LSEM V44 after dual-beam ion irradiation at 700 C (A). Insets show hardness maps (not to scale) with the hardness value in GPa of the areas indicated by the colored rectangles (to scale). (B) shows a plot of the average hardness at an arbitrary distance away from the center perforation hole from each of the hardness map areas. The gray dashed line represents the distance cut-off, after which the hardness values begin to stabilize and are used for the average hardness value of the ion irradiated specimen.

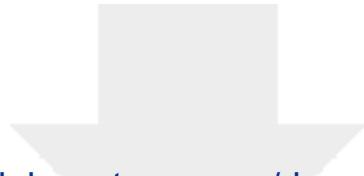


[Click here to access/download](#)

**Supplementary Material**

V44\_NC\_EP\_ion irradiation\_43 s.mp4

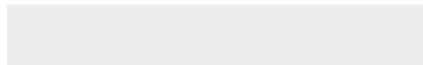


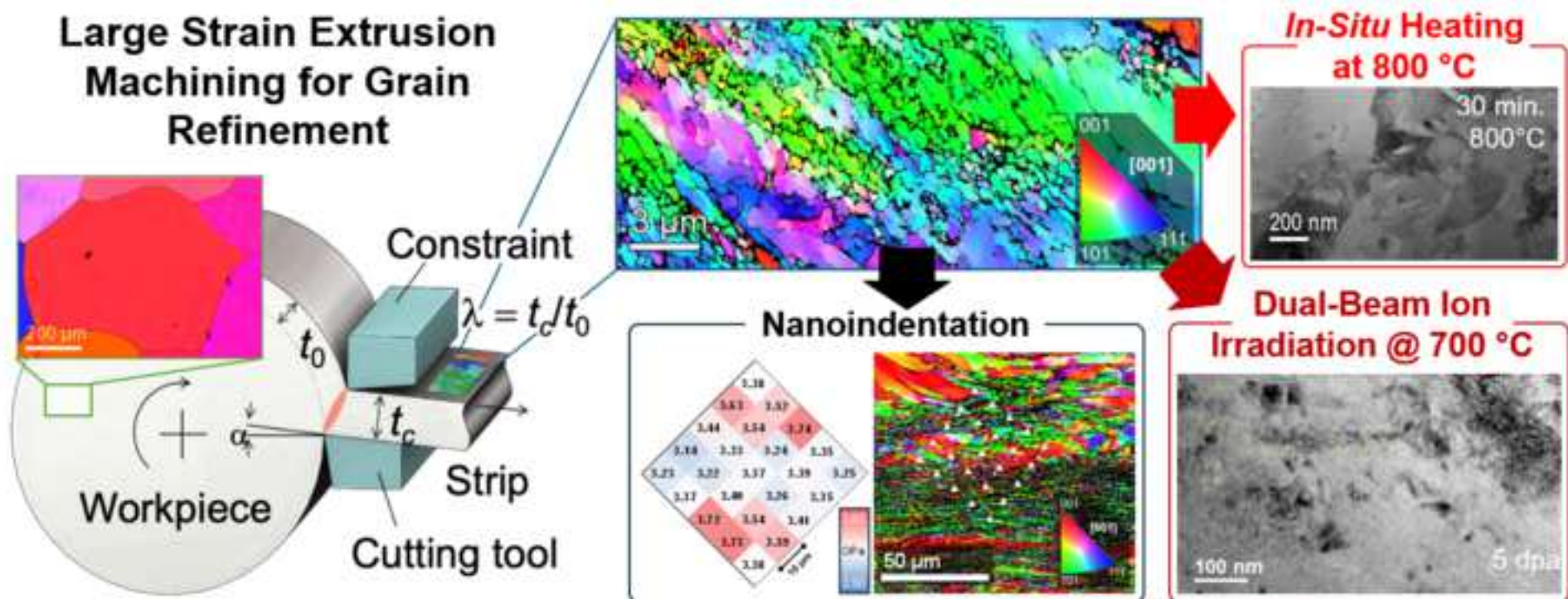


[Click here to access/download](#)

**Supplementary Material**

V44 Cg Dim Ion Irradiation\_50mb.mp4





**Declaration of interests**

The authors declare that they have no known competing financial interests or personal relationships that could have appeared to influence the work reported in this paper.

The authors declare the following financial interests/personal relationships which may be considered as potential competing interests: